

CETASim: A numerical tool for beam collective effect study in storage rings

Chao Li* and Yong-Chul Chae†

Deutsches Elektronen Synchrotron, Notkestrasse 85, 22607, Hamburg, Germany

(Dated: December 13, 2023)

Abstract

We developed a 6D multi-particle tracking program CETASim in C++ programming language to simulate intensity-dependent effects in electron storage rings. The program can simulate the collective effects due to short-range and long-range wakefields for single and coupled-bunch instability studies. It also features to simulate the ion interactions with the trains of electron bunches, including both fast ion and ion trapping effects. As an accelerator design tool, the bunch-by-bunch feedback is also included so that the user can simulate the damping of the unstable motion when its growth rate is faster than the radiation damping rate. The particle dynamics is based on the one-turn map, including the nonlinear effects of amplitude-dependent tune shift, high-order chromaticity, and second-order momentum compaction factor. When required, a skew quadrupole can also be introduced, which is very useful for the emittance sharing and the emittance exchange studies. This paper describes the code structure, the physics models, and the algorithms used in CETASim. We also present the results of its application to the PETRA-IV storage ring.

PACS numbers: 41.75.-i, 29.27.Bd, 29.20.Ej

Key words: electron storage rings, beam collective effect, impedance and wakefield, CETASim

1. INTRODUCTION

The 4th generation light sources move towards a diffraction-limited storage ring (DLSR) where the intense bunched beam with ultra-small emittance is stored for many hours for X-ray user operations. Because of the small beam dimensions with appreciable beam intensities, various collective effects will limit the performance of the ring in delivering the optimum beam parameters for user operations. Traditionally, the short and long-range wakefield effects are the leading cause of instability we need to mitigate; however, we found that the ion, beam loading, transverse coupling, and other effects will impact the beam parameters significantly when considering the intrabeam scattering effect. Since the Touschek lifetime impacts a whole aspect of operation, predicting and improving the lifetime becomes vital. These require investigating advanced beam dynamics caused by collective effects.

Multi-particle tracking has been a popular method to investigate the collective effects in the electron storage rings; various codes have been developed including ELEGANT [1], MBTRACK [2], and PyHEADTAIL [3] *etc.* The benchmark between the codes is an ongoing effort in the light source communities. The motivation for developing CETASim is to have a light and user-friendly tool, which includes the fundamental physics of various collective effects and approaches for instability mitigation. It is also beneficial for future studies since CETASim can be updated and upgraded appropriately when new physics needs arise. The remainder of this paper is organized as follows. In Section 2, the architecture of the code is introduced. Section 3 explains the physics models and algorithms for various collective effects used in CETASim. Section 4 showed a few result from PETRA-IV storage ring as a demonstration of CETASim. Summary and conclusions are given in the end.

2. GENERAL CODE OVERVIEW

We developed CETASim following object-oriented concepts in C++ programming language. Fig. 1 shows the main classes designed. The program generates the specified bunch train and launches the particle tracking task using the input parameters in the run setup. For the multi-bunch problem, the users can set each bunch charge individually while keeping the number of macro-particles per bunch constant. It is a handy feature for investigating

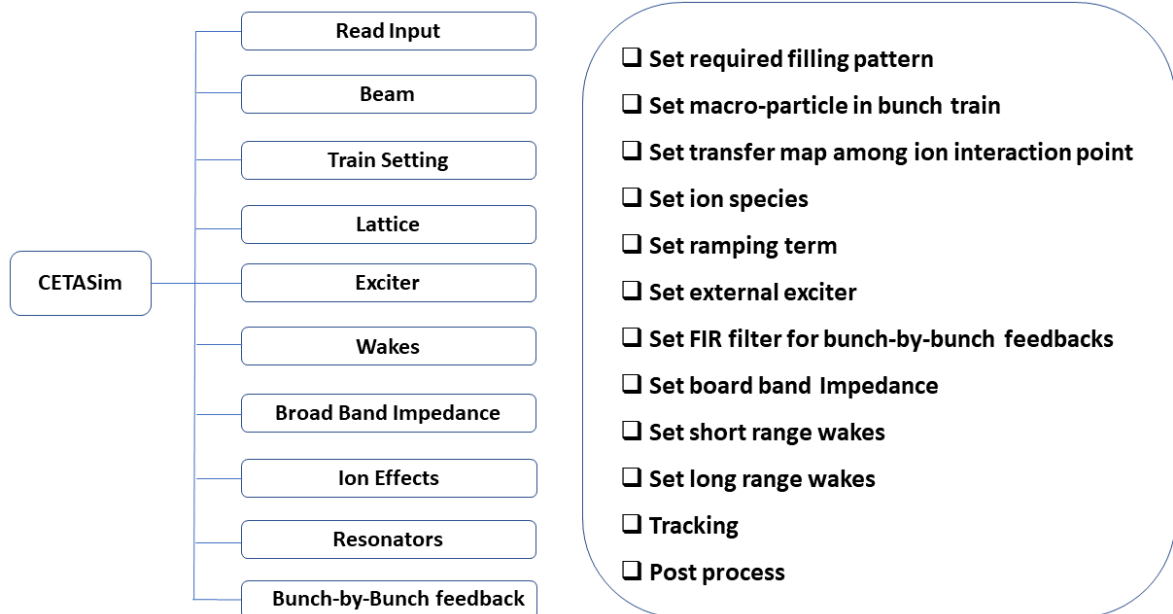


FIG. 1. General overview of the code CETASim.

transient beam loading compensation and ion cleaning with guarding bunches. Investigating ion effects, the code can have multiple beam-ion interactions in the ring. Numerous ion species, local gas temperatures, and pressures can be set independently at each interaction point. The impedance class will use the analytical formula to construct the model ring impedance for the resistive wall and resonator model. Otherwise, it will import impedance data from an external file. Besides the impedance and wake class, the exciter class can apply an external drive signal to the electron bunches with a given frequency, which plays as a coupled bunch mode driver in the "drive-damp" simulation. As a particular case of the longitudinal coupled bunch motion, the transient beam loading effect is dealt with within the resonator class. The cavity dynamics, which is driven by the generator current and the beam current, together with the beam dynamics are simulated simultaneously in a self-consistent manner. We plan to implement the cavity feedback to stabilize the cavity voltage based on the control parameters in the future. The bunch-by-bunch feedback class simulates *Finite Impulse Response* (FIR) filter to compute the kicker response based on the multi-turn beam position monitor (BPM) data. The data output uses the SDDS format, which can be post-processed by the SDDS toolkit [4].

3. PHYSICAL MODELS IN CETASIM

In CETASim the position of every macro-particle is described by a 6D vector $\mathbf{x} = (x, p_x, y, p_y, dz, \delta)$ in phase space, where x and y are particle positions in the horizontal and vertical directions, p_x and p_y are the transverse momentum normalized by the reference momentum p_0 ; whereas dz and $\delta = (p - p_0)/p_0$ are the longitudinal positions and momentum deviation with respect to the reference particle. The sign convention is such that the head of the particles has a positive distance, namely, $dz > 0$. If time-dependent elements are included, such as RF cavities, dz is converted to the time deviation by $d\tau = -dz/\beta c$ to compute the RF phase, where β is the relativity factor and c is the speed of light.

3.1 Beam transfer in one turn

3.1.1 The longitudinal beam transformation

The longitudinal dynamics is described by the transfer map given by

$$dz_{i+1} = dz_i - L \sum_{j=1}^3 \alpha_{cj} (\delta_i)^j \quad d\delta_{i+1} = d\delta_i + \frac{1}{\beta^2 E_0} (-U_0 + \sum_n e V_{n,rf} \sin(\omega_{n,rf} d\tau_i + \phi_n)), \quad (1)$$

where α_{cj} is the j th order of momentum compaction factor, U_0 is the energy loss per turn due to the synchrotron radiation, n is the cavity index, $V_{n,rf}$, $\omega_{n,rf}$ and ϕ_n are the cavity voltage, angular frequency and phase respectively, and e is the electron charge.

3.1.2 The transverse beam transformation

The one-turn matrix \mathbf{R} is given by

$$\mathbf{R} = \begin{pmatrix} \cos \psi_x + \alpha_x \sin \psi_x & \beta_x \sin \psi_x & 0 & 0 & 0 & R_{16} \\ -\gamma_x \sin \psi_x & \cos \psi_x - \alpha_x \sin \psi_x & 0 & 0 & 0 & R_{26} \\ 0 & 0 & \cos \psi_y + \alpha_y \sin \psi_y & \beta_y \sin \psi_y & 0 & R_{36} \\ 0 & 0 & -\gamma_y \sin \psi_y & \cos \psi_y - \alpha_y \sin \psi_y & 0 & R_{46} \\ R_{51} & R_{52} & R_{53} & R_{54} & 1 & 0 \\ 0 & 0 & 0 & 0 & 0 & 1 \end{pmatrix}, \quad (2)$$

where $\alpha_{(x,y)}$, $\beta_{(x,y)}$ and $\gamma_{(x,y)}$ are the Twiss parameters and R_{ij} are dispersion related functions, which ensures the orbit is closed. $\psi_{(x,y)}$ is the phase advance per turn, including the contribution from chromaticity and amplitude-dependent tune shift. We note that $R_{55} = R_{66} = 1$, and deal with the longitudinal dynamics separately.

For the beam-ion interaction, users can split the ring into several sections to set up multiple beam-ion interaction points. If in this case, a simpler transfer matrix is adopted for each plane given as

$$\mathbf{R}_x = \begin{pmatrix} \sqrt{\frac{\beta_{x,i+1}}{\beta_{x,i}}}(\cos \psi_{xi} + \alpha_{x,i} \sin \psi_{xi}) & \sqrt{\beta_{x,i+1}\beta_{x,i}} \sin \psi_{xi} & \eta_{xi} \\ -\frac{1+\alpha_{x,i+1}\alpha_{x,i}}{\sqrt{\beta_{x,i+1}\beta_{x,i}}} \sin \psi_{xi} + \frac{\alpha_{x,i}-\alpha_{x,i+1}}{\sqrt{\beta_{x,i+1}\beta_{x,i}}} \cos \psi_{xi} & \sqrt{\frac{\beta_{x,i}}{\beta_{x,i+1}}}(\cos \psi_{xi} - \alpha_{x,i+1} \sin \psi_{xi}) & \eta'_{xi} \\ 0 & 0 & 1 \end{pmatrix} \quad (3)$$

where α_{xi} , β_{xi} , ψ_{xi} are the local Twiss parameters and phase advance, η_{xi} , η'_{xi} are the dispersion functions. The transfer map \mathbf{R}_y in the vertical plane is obtained similarly.

3.1.3 synchrotron radiation and quantum excitation

We follow the approach developed by Hirata [5] to include the synchrotron radiation and quantum excitation to get to the 6-D equilibrium emittances. To do that, we normalize the accelerator coordinate vector \mathbf{x} to normal frame \mathbf{X} by using dispersion matrix \mathbf{H} and Twiss matrix \mathbf{B}

$$\mathbf{X} = \mathbf{BHx}. \quad (4)$$

The dispersion matrix \mathbf{H} is defined as

$$\mathbf{H} = \begin{pmatrix} \mathbf{I} & 0 & -\mathbf{H}_x \\ 0 & \mathbf{I} & -\mathbf{H}_y \\ -\mathbf{J}_2 \mathbf{H}_x^T \mathbf{J}_2 & -\mathbf{J}_2 \mathbf{H}_y^T \mathbf{J}_2 & \mathbf{I} \end{pmatrix} \quad (5)$$

where

$$\mathbf{H}_x = \begin{pmatrix} 0 & \eta_x \\ 0 & \eta'_x \end{pmatrix}, \quad \mathbf{H}_y = \begin{pmatrix} 0 & \eta_y \\ 0 & \eta'_y \end{pmatrix}, \quad \mathbf{J}_2 = \begin{pmatrix} 0 & -1 \\ -1 & 0 \end{pmatrix}. \quad (6)$$

The Twiss matrix \mathbf{B} is defined as

$$\mathbf{B} = \begin{pmatrix} \frac{1}{\sqrt{\beta_x}} & 0 & 0 & 0 & 0 & 0 \\ \frac{\alpha_x}{\sqrt{\beta_x}} & \sqrt{\beta_x} & 0 & 0 & 0 & 0 \\ 0 & 0 & \frac{1}{\sqrt{\beta_y}} & 0 & 0 & 0 \\ 0 & 0 & \frac{\alpha_y}{\sqrt{\beta_y}} & \sqrt{\beta_y} & 0 & 0 \\ 0 & 0 & 0 & 0 & \frac{1}{\sqrt{\beta_z}} & 0 \\ 0 & 0 & 0 & 0 & \frac{\alpha_z}{\sqrt{\beta_z}} & \sqrt{\beta_z}. \end{pmatrix} \quad (7)$$

In CETASim, α_z is assumed to be zero and $\beta_z = \sigma_z/\sigma_e$, where σ_z and σ_e are the natural bunch length and energy spread. Thereafter, the effect of synchrotron radiation and quantum excitation is simulated in the normalized frame \mathbf{X} according to

$$\begin{aligned} \begin{pmatrix} \mathbf{X}_1 \\ \mathbf{X}_1 \end{pmatrix} &= \lambda_x \begin{pmatrix} \mathbf{X}_1 \\ \mathbf{X}_1 \end{pmatrix} + \sqrt{\epsilon_x(1 - \lambda_x^2)} \begin{pmatrix} \hat{r}_1 \\ \hat{r}_2 \end{pmatrix} \\ \begin{pmatrix} \mathbf{X}_3 \\ \mathbf{X}_4 \end{pmatrix} &= \lambda_y \begin{pmatrix} \mathbf{X}_3 \\ \mathbf{X}_4 \end{pmatrix} + \sqrt{\epsilon_y(1 - \lambda_y^2)} \begin{pmatrix} \hat{r}_3 \\ \hat{r}_4 \end{pmatrix} \\ \begin{pmatrix} \mathbf{X}_5 \\ \mathbf{X}_6 \end{pmatrix} &= \begin{pmatrix} 1 & 0 \\ 0 & \lambda_z^2 \end{pmatrix} \begin{pmatrix} \mathbf{X}_5 \\ \mathbf{X}_6 \end{pmatrix} + \begin{pmatrix} 0 \\ \sqrt{\epsilon_z(1 - \lambda_z^4)} \end{pmatrix} \begin{pmatrix} 0 \\ \hat{r}_6 \end{pmatrix}, \end{aligned} \quad (8)$$

once per turn. Here \hat{r} is an independent Gaussian random variables with unit variance; $\lambda_{x,y,z} = \exp(-1/\tau_{x,y,z})$ is the transport coefficient with $\tau_{x,y,z}$ representing the synchrotron radiation damping time in the units of the number of turns; ϵ_x , ϵ_y and ϵ_z are the equilibrium beam emittance, where $\epsilon_z = \sigma_z\sigma_e$. Once the synchrotron radiation and quantum excitation simulation is done, the normalized \mathbf{X} is transformed back to \mathbf{x} by

$$\mathbf{x} = \mathbf{H}^{-1}\mathbf{B}^{-1}\mathbf{X}. \quad (9)$$

3.2 Impedance and wakes models in CETASim

Impedance in the frequency domain and wakes in the time domain describe the same physics. In CETASim, the single bunch effect uses the impedance to compute the wake potential in the bunch to simulate the single-bunch collective effects; the coupled bunch effect is simulated directly in the time domain by using the known formula of resistive-wall and resonator wakes. The impedance data can be generated from analytical models or

read from an external file. The resistive wall and a resonator impedance are presented as referenced to Ref. [6].

3.2.1 RLC impedance and wake

Equation 10 gives the impedance of the RLC circuit as a function of angular frequency ω ,

$$Z_m^{\parallel}(\omega) = \frac{\omega}{c} Z_m^{\perp}(\omega) = \frac{R_s}{1 + iQ\left(\frac{\omega_r}{\omega} - \frac{\omega}{\omega_r}\right)}, \quad (10)$$

where R_s is the resistance with a dimension Ω/L^{2m} , Q is the quality factor, ω_r is the resonant angular frequency. Correspondingly, the longitudinal ($W'_m(z)$) and the transverse ($W_m(z)$) wake functions are

$$W'_m(z) = \begin{cases} 0 & z > 0 \\ \frac{R_s}{\tau_f} & z = 0 \\ 2\frac{R_s}{\tau_f} e^{z/c\tau_f} \left(\cos \frac{\bar{\omega}z}{c} + \frac{1}{\bar{\omega}\tau_f} \sin \frac{\bar{\omega}z}{c} \right) & z < 0, \end{cases} \quad (11)$$

$$W_m(z) = \begin{cases} 0 & z = 0 \\ \frac{cR_s\omega_r}{2Q} e^{z/c\tau_f} \sin \frac{\bar{\omega}z}{c} & z <= 0, \end{cases}$$

where $\tau_f = 2Q/\omega_r$ representing the filling or damping time in the circuit and $\bar{\omega} = \sqrt{\omega_r^2 - 1/\tau_f^2}$.

3.2.2 Resistive wall impedance and wake

The resistive wall (RW) impedance from a infinitely thick metallic round beam pipe of radius b and conductivity σ is well-known. When the beam pipe has an elliptical shape, Yokoya factors [7] can be applied. Eq. 12 shows the model of RW impedance per unit length as a function of angular frequency ω

$$Z_m^{\parallel}(\omega) = \frac{\omega}{c} Z_m^{\perp}(\omega) = \frac{4/b^{2m}}{(1 + \delta_{m0})bc\sqrt{\frac{2\pi\sigma}{|\omega|}}[1 + sgn(\omega)i] - \frac{ib^2}{m+1}\omega + \frac{imc^2}{\omega}} \quad (12)$$

$$\approx \sqrt{\frac{2}{\pi\sigma}} \frac{1}{(1 + \delta_{m0})b^{2m+1}c} |\omega| [1 - sgn(\omega)i],$$

where $\delta_{m,0}$ is the Kronecker-Delta function, i is the imaginary unit, sgn is the *Sign* function. Limiting the RW impedance to the lowest order $m = 0, 1$ in the longitudinal and transversely

respectively, the longitudinal and transverse wake functions can be obtained by the Fourier transform. Define $z_0 = (2\chi)^{1/3}b$ as the characteristic distance, where $\chi = c/(4\pi\sigma b)$ is a dimensionless parameter, the longitudinal and transverse RW wakes are expressed as [2]:

$$\begin{aligned} W'_0(z) &= \frac{1}{b^2} \left[\frac{e^{-z/z_0}}{3} \cos\left(\frac{\sqrt{3}z}{z_0}\right) - \frac{\sqrt{2}}{\pi} \int_0^\infty dx \frac{x^2 e^{-x^2 z/z_0}}{x^6 + 8} \right] \\ W_1(z) &= -\frac{32}{b^3} (2\chi)^{1/3} \left[\frac{e^{-z/z_0}}{12} \cos\left(\frac{\sqrt{3}z}{z_0}\right) - \frac{1}{4\sqrt{3}} e^{-z/z_0} \sin\left(\frac{\sqrt{3}z}{z_0}\right) - \frac{\sqrt{2}}{\pi} \int_0^\infty dx \frac{x^2 e^{-x^2 z/z_0}}{x^6 + 8} \right]. \end{aligned} \quad (13)$$

If the simplified RW impedance is adopted in Eq. 12, the RW wakes are simplified further to

$$W'_0(z) \approx \frac{1}{2\pi b} \sqrt{\frac{c}{\sigma}} \frac{1}{|z|^{3/2}} \quad W_1(z) \approx -\frac{2}{\pi b^3} \sqrt{\frac{c}{\sigma}} \frac{1}{|z|^{1/2}}. \quad (14)$$

Figure 2 compares the exact (Eq. 13) and approximate solution (Eq. 14) of the RW impedance and wakes. In terms of impedance, the discrepancy exists both in the low and high-frequency regions. The results from the exact and the approximated solutions are basically the same in the medium frequency region. The wakes from the exact and approximate solutions agree well when $u = |z|/z_0 > 5$. Since the distance among different bunches is much longer than the characteristic distance z_0 , the asymptotic wake Eq. 14 is applied in CETASim for the coupled-bunched simulation to relax the computation load.

3.3 Single bunch effect

The energy change within the bunch caused by the longitudinal wake can be expressed as

$$eV^{\parallel}(z) = -e \int_z^\infty \rho(z') W'_0(z-z') dz' = -\frac{e}{2\pi} \int_{-\infty}^\infty e^{i\omega z/c} \tilde{\rho}(\omega) Z_0^{\parallel}(\omega) d\omega, \quad (15)$$

where $\tilde{\rho}(\omega)$ is the charge-density in the frequency domain. In the transverse planes, we consider the dipole W_1^D and quadrupole W_1^Q wakes, the impedance of which is denoted as $Z_1^D(\omega)$ and $Z_1^Q(\omega)$, respectively. The kick in the transverse plane within the bunch can be expressed as

$$\begin{aligned} eV^{\perp}(z) &= -e \int_z^\infty \rho(z') x(z') W_1^D(z-z') dz' - e \int_z^\infty \rho(z') x(z) W_1^Q(z-z') dz' \\ &= -i \frac{e}{2\pi} \int_{-\infty}^\infty e^{i\omega z/c} \tilde{\rho}^D(\omega) Z_1^D(\omega) d\omega - i \frac{e}{2\pi} x(z) \int_{-\infty}^\infty e^{i\omega z/c} \tilde{\rho}(\omega) Z_1^Q(\omega) d\omega, \end{aligned} \quad (16)$$

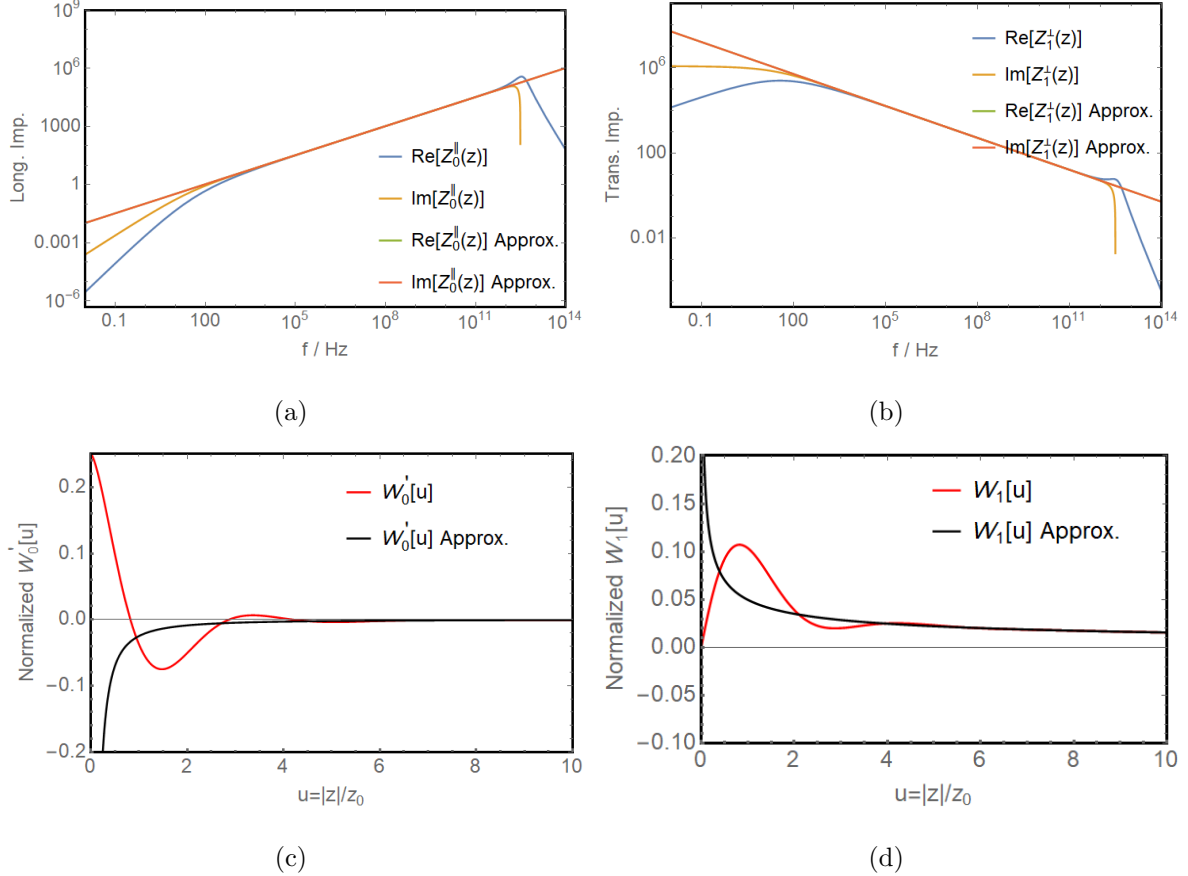


FIG. 2. Comparison of the exact and approximated solutions of the resistive impedance (above) and wakes (bottom). The sub-figures on the left and right correspond to the lowest order of the longitudinal and transverse respectively.

where, $x(z)$ is the transverse position offset along the beam, $\tilde{\rho}^D(\omega)$ is the spectrum of the dipole moment $\rho(z)x(z)$.

In CETASim, Eq. 15 and Eq. 16 in the frequency domain are used to compute $eV^{\parallel}(z)$ and $eV^{\perp}(z)$ within the bunch. In time domain approach of the same equations, we plan to read the wake directly from the user-supplied data to compute the kicks. Until then we rely on the analytic formula of resistive wall and resonator wakes to compute the bunch potentials.

3.4 Coupled bunch effect

If the wakefield generated by resistive-wall and high-Q resonators lasts longer than the bunch spacing, then the motion of bunches will be coupled. Assuming there are N_b bunches in total in the ring, the kick at the j th bunch at the n th turn from the longitudinal wakes

W'_0 and transverse dipole (W_1^D) and quadrupole wakes (W_1^Q) can be expressed as

$$\begin{aligned}\Delta p_{z;n}^j &\sim \sum_{k=0}^{n-1} \sum_{i=0}^{Nb-1} W'_0(hcT_{rf}(n-k) + \delta s_{i;j}) \\ \Delta p_{x;n}^j &\sim \sum_{k=0}^{n-1} \sum_{i=0}^{Nb-1} [\langle x \rangle_k^i W_1^D(hcT_{rf}(n-k) + \delta s_{i;j}) + \langle x \rangle_0^j W_1^Q(hcT_{rf}(n-k) + \delta s_{i;j})], \quad (17) \\ \delta s_{i;j} &= \begin{cases} (i-j)cT_{rf} & j \leq i \\ (i-j+h)cT_{rf} & j > i \end{cases}\end{aligned}$$

where h is the RF harmonic number, T_{rf} is the RF period, $\langle x \rangle_k^i$ is bunch centroid of the i th bunch at k th previous turn. CETASim can simulate the long-range wakes from the RW (Eq. 11) and RLC (Eq. 14) elements. How long the long wakes last can be specified by the users in the unit of number of turns.

3.5 Bunch-by-bunch feedback

The bunch-by-bunch feedback can mitigate the coupled bunch instabilities. It detects the transverse or longitudinal positions and creates the kicker signal, processing the position signal by a digital filter, to damp the bunch oscillations. The FIR filter used for that purpose can be expressed as

$$\Theta_n = \sum_{k=0}^N a_k \theta_{n-k} \quad (18)$$

where a_k represents the filter coefficient, θ_{n-k} and Θ_n are the input and output digital signal of the filter. The number of the input data $N+1$ is defined as the taps of the filter. With a given FIR filter, the bunch momentum change at the kicker in the n th turn due to the bunch-by-bunch feedback can be found

$$\Delta p_{x;n} \sim K_x \sum_{k=0}^N a_{k,x} \langle x \rangle_{n-k}, \quad \Delta p_{y;n} \sim K_y \sum_{k=0}^N a_{k,y} \langle y \rangle_{n-k}, \quad \Delta \delta_n \sim K_z \sum_{k=0}^N a_{k,z} \langle z \rangle_{n-k}, \quad (19)$$

where $\langle x, y, z \rangle_{n-k}$, are the bunch centroids of the k th previous turn at the pickup; $K_{x,y,z}$ is the gain factor. The power constraints and kicker impedance limit the maximum momentum change. Particles in the bunch will get the same kick from the device with the finite bandwidth much narrower than the bunch spectrum.

3.6 Beam-ion effect

The program simulate the Coulomb interaction between the electron bunch and the ionized gases. In an accelerator, if the gas pressure P and temperature T are given, the number of ionized gases can be estimated by

$$\Lambda = \Sigma \frac{PN_A}{RT} N_b, \quad (20)$$

where Σ is the ionization collision cross-section, N_b is the number of electron particles, R the ideal gas constant and N_A is the Avogadro constant. The ions can be locally trapped by passing electron bunches acting as the focusing lenses. The trapping condition can be expressed as

$$A \geq A_c = \frac{QN_b r_p \Delta T_b c}{2\sigma_y(\sigma_x + \sigma_y)} \quad (21)$$

where A is the ion mass, Q is the ion charge number, r_p is the classical radius of the proton, ΔT_b is the bunch separation in time. Only the ions with a mass number larger than the critical mass number A_c can be trapped. This formula assumes a linear focusing and uniform fill pattern. We note that the critical ion mass A_c varies following the betatron function around the ring.

In CETASim, we assume the electron bunch has a rigid Gaussian distribution represented by a single particle. The 2D *Bassetti – Erskine* formula [8] is applied at the interaction point s_i to get the beam ion interaction force

$$\begin{aligned} \mathbf{F}(\mathbf{x}, \mathbf{y})_y + i\mathbf{F}(\mathbf{x}, \mathbf{y})_x &= \delta(s_i) \sqrt{\frac{\pi}{2(\sigma_x^2 - \sigma_y^2)}} \\ &\{ w\left(\frac{x+iy}{\sqrt{2\pi(\sigma_x^2 - \sigma_y^2)}}\right) - \exp\left(-\frac{x^2}{2\sigma_x^2} - \frac{y^2}{2\sigma_y^2}\right) w\left(\frac{x\frac{\sigma_y}{\sigma_x} + iy\frac{\sigma_x}{\sigma_y}}{\sqrt{2\pi(\sigma_x^2 - \sigma_y^2)}}\right) \}, \end{aligned} \quad (22)$$

where $w(z)$ is the complex error function, σ_x and σ_y are the rms bunch size [9]. If there are N_i ionized ions accumulated already, the motion for the electrons and ions can be expressed by

$$\begin{aligned} \frac{d^2\langle \mathbf{x} \rangle}{ds^2} + K_e(s)\langle \mathbf{x} \rangle &= \frac{2r_e}{\gamma} \sum_{i=0}^{N_i} \mathbf{F}(\langle \mathbf{x} \rangle - \mathbf{X}_i), \\ \frac{d^2\mathbf{X}_i}{dt^2} &= \frac{2N_b r_e c^2}{M_i/m_e} \sum_{j=0}^{N_b} \mathbf{F}(\mathbf{X}_i - \langle \mathbf{x} \rangle) \end{aligned} \quad (23)$$

where $\mathbf{X}_i = (x, y)_i$ is the ion position, $\langle \mathbf{x} \rangle = (\langle x \rangle, \langle y \rangle)$ is the bunch centroids, \mathbf{F} is the Coulomb force between the ions and electron particles, K_e represent the external focusing strength on electron particles, r_e is the classical electron radius, γ is the relativistic factor of electron beam, M_i and m_e are the mass of ion and electron. This model assumes that the electron bunch is rigid, i.e. a weak-strong model. If the motion of individual electrons are important, one can assume that the ions form a rigid Gaussian distribution as well. Then the Coulomb force from the ions on individual electron particle can be obtained similarly, i.e. a quasi "strong-strong" model. In CETASim, both the "weak-strong" and quasi "strong-strong" model are available to use in simulation.

3.7 Beam loading effect and cavity feedback

The discussion of the transient beam loading effect refers to the fundamental mode of RF cavities. As usual, the fundamental mode of the cavity is modeled as an RLC circuit, where the generator dynamics and beam dynamics are coupled. Following the previous discussion and combining Eq. 11 and Eq. 17, if the cavity is passive, the beam motion can be simulated self-consistently. However, the price is that the history of previous bunches has to be kept in memory. In a ring with multipole RF systems, at least the main cavity has to be active, which brings additional complexity to the whole study, especially when the cavity feedback has to be included further.

In CETASim, we follow the approaches of P.B. Wilson [10], solving the coupled dynamics in the phasor diagram. The total cavity voltage $\tilde{\mathbf{V}}_c(t)$, that the beam can sample as a function of time t , can be expressed as the sum of the generator voltage $\tilde{\mathbf{V}}_g(t)$ and beam induced voltage $\tilde{\mathbf{V}}_b(t)$,

$$\tilde{\mathbf{V}}_c(t) = \tilde{\mathbf{V}}_g(t) + \tilde{\mathbf{V}}_b(t). \quad (24)$$

Noticeably, $\tilde{\mathbf{V}}_b(t)$ and $\tilde{\mathbf{V}}_g(t)$ are driven by the beam current $\tilde{\mathbf{I}}_b(t)$ and the generator current $\tilde{\mathbf{I}}_g(t)$ respectively. The information of the long-range wakes is stored in the beam induced voltage $\tilde{\mathbf{V}}_b(t)$. With the RLC circuit model, the resonant voltage excited by a driving current $\tilde{\mathbf{I}}(t)$ follows the differential equation [11]

$$\frac{d^2}{dt^2} \tilde{\mathbf{V}}(t) + \frac{\omega_r}{Q_L} \frac{d}{dt} \tilde{\mathbf{V}}(t) + \omega_r^2 \tilde{\mathbf{V}}(t) = \frac{\omega_r R_L}{Q_L} \frac{d}{dt} \tilde{\mathbf{I}}(t), \quad (25)$$

where Q_L and R_L are the loaded quality factor and shunt impedance.

Note ω_{rf} as the angular frequency of the driving term $\tilde{\mathbf{I}}(t)$, if several conditions are meet: (1) the second order terms can be neglected [12]; (2) $Q_L \gg 1$; (3) $\Delta\omega = \omega_r - \omega_{rf} \ll \omega_r$, together with the zero order hold method, the solution of Eq. 25 can be further simplified in the state space [11, 13]

$$\begin{pmatrix} V^r \\ V^i \end{pmatrix}_{n+1} = e^{-\omega_{1/2}\Delta T} \begin{pmatrix} \cos \Delta\omega \Delta T & -\sin \Delta\omega \Delta T \\ \sin \Delta\omega \Delta T & \cos \Delta\omega \Delta T \end{pmatrix} \begin{pmatrix} V^r \\ V^i \end{pmatrix}_n + \frac{\omega_r R_L}{2Q_L(\omega_{1/2}^2 + \Delta\omega^2)} \begin{pmatrix} A & B \\ -B & A \end{pmatrix} \begin{pmatrix} I^r \\ I^i \end{pmatrix}_n \quad (26)$$

where $\omega_{1/2} = 1/\tau_f$, ΔT is the time step, A and B are

$$\begin{aligned} A &= \Delta\omega e^{-\omega_{1/2}\Delta T} \sin \omega_{1/2} \Delta T - \omega_{1/2} e^{-\omega_{1/2}\Delta T} \cos \omega_{1/2} \Delta T + \omega_{1/2} \\ B &= \omega_{1/2} \omega e^{-\omega_{1/2}\Delta T} \sin \omega_{1/2} \Delta T + \Delta\omega e^{-\omega_{1/2}\Delta T} \cos \omega_{1/2} \Delta T - \Delta\omega. \end{aligned} \quad (27)$$

The generator current $\tilde{\mathbf{I}}_g(t)$ is continuous and has a angular frequency ω_{rf} . Numerically, for a given initial driving current $\tilde{\mathbf{I}}_g(\mathbf{0})$, Eq. 26 can be solved to obtain $\tilde{\mathbf{V}}_g(\mathbf{t})$ step by step in time domain. It is referenced as the generator dynamics and still available when there exists feedback current $\delta\tilde{\mathbf{I}}_g(\mathbf{t})$.

The beam current $\tilde{\mathbf{I}}_b(t)$ is discrete and can be expressed as

$$\tilde{\mathbf{I}}_b(t) \propto \sum_{k=-\infty}^{k=\infty} \delta(t - kT_{rf}) = I_{DC} + 2I_{DC} \sum_{k=1}^{k=\infty} \exp(ik\omega t), \quad (28)$$

where I_{DC} is the DC (average) beam current. The driving current in the resonant cavity from the beam is actually the image current of $\tilde{\mathbf{I}}_b(t)$. Only the frequency component at ω_{rf} is synchronized with the bunch repetition rate, then the driving current due to beam can be further simplified to $-2I_{DC} \exp(i\omega_{rf}t)$. Similarly, the beam induced voltage $\tilde{\mathbf{V}}_b(\mathbf{t})$ can be obtained by solving Eq. 25. However, from the fundamental theory of beam loading, this process can be significantly simplified. Assume there is a bunch with charge q passing through the cavity at time $t - \Delta t$, then the beam induced voltage satisfies,

$$\tilde{\mathbf{V}}_b(t) = (\tilde{\mathbf{V}}_b(t - \Delta t) + \tilde{\mathbf{V}}_{b0}/2) \exp(\alpha\Delta t), \quad \alpha = -\frac{1}{\tau_f}(1 - i \tan \Psi) \quad (29)$$

where Δt is the time distance between charged bunches, Ψ is the cavity de-tuning angle. The phase and amplitude of the beam induced voltage $\tilde{\mathbf{V}}_{b0}/2$ is π and $|\tilde{\mathbf{V}}_{b0}| = q\omega_r R_L / Q_L$.

Clearly, the accumulated beam induced voltage $\tilde{\mathbf{V}}_{\mathbf{b}}(t)$ adds an impulse $\tilde{\mathbf{V}}_{\mathbf{b}0}/2$ whenever a charged bunch passes by, then it decays and rotates by a factor of $\exp(\alpha\Delta t)$ until the next bunch comes. Clearly, the simulation does not require bunch information from the previous turns, which dramatically lowers the computational effort.

In an accelerator with the multi-RFs, the total cavity voltage [14] the beam samples usually deviates from the designed value due to the beam induced voltage, especially when the ring is non-uniform filled,

$$\begin{aligned}\tilde{\mathbf{V}}_{\mathbf{c}}(\mathbf{t}) &= \sum_n \tilde{\mathbf{V}}_{\mathbf{c},n}(t) = \sum_n (\tilde{\mathbf{V}}_{\mathbf{g},n}(t) + \tilde{\mathbf{V}}_{\mathbf{b},n}(t)) \\ &\neq \sum_n \tilde{V}_{c,n}^{set} = \sum_n V_{c,n}^{set} \exp(i\omega_{rf,n}t + \phi_n).\end{aligned}\quad (30)$$

Different bunches will sample different cavity voltages and phases. Thus, cavity feedforward or feedback, are required to compensate the transient beam loading effect. Fig. 3 shows a loop of cavity feedback at the generator side. The performance of the cavity feedback systems is determined by the cavity phasor measurement $\tilde{\mathbf{V}}_{\mathbf{c},n}(t)$ sampling at the RF cycle $t = mT_{rf}$. The cavity feedback filter can be a *Finite Impulse Response* (FIR) or a *Infinite Impulse Response* (IIR) types, which takes the generator current $\tilde{\mathbf{I}}_{\mathbf{g},n}(t)$ and cavity voltage error $\delta\tilde{\mathbf{V}}(t) = \tilde{\mathbf{V}}_{\mathbf{c},n}^{set}(t) - \tilde{\mathbf{V}}_{\mathbf{c},n}(t)$ as input and gives $\delta\tilde{\mathbf{I}}_{\mathbf{g}}(t)$ to be modified at the generator side as output. Explicitly, the cavity feedback can be expressed as

$$\delta\tilde{\mathbf{I}}_{\mathbf{g}}(nT_{rf}) = -\frac{1}{a_0} \sum_{i=1}^N a_i \delta\tilde{\mathbf{I}}_{\mathbf{g}}((n-i)T_{rf}) + \frac{1}{b_0} \sum_{j=0}^M b_j \delta\tilde{\mathbf{V}}((n-j)T_{rf}) \quad (31)$$

where $\delta\tilde{\mathbf{I}}_{\mathbf{g},n}(t)$ and $\delta\tilde{\mathbf{V}}(t)$ are the filter output and input.

Finally, we summarize steps for the transient beam loading effect simulation,

1. Solve Eq. 26 to get the $\tilde{\mathbf{V}}_{\mathbf{g},n}(t)$.
2. Solve Eq. 29 to get the $\tilde{\mathbf{V}}_{\mathbf{b},n}(t)$.
3. Solve Eq. 30 to get the $\tilde{\mathbf{V}}_{\mathbf{c},n}(t)$.
4. Transfer the particle by the one-turn map
5. Solve Eq. 31 to get the $\delta\tilde{\mathbf{I}}_{\mathbf{g},n}(t)$.

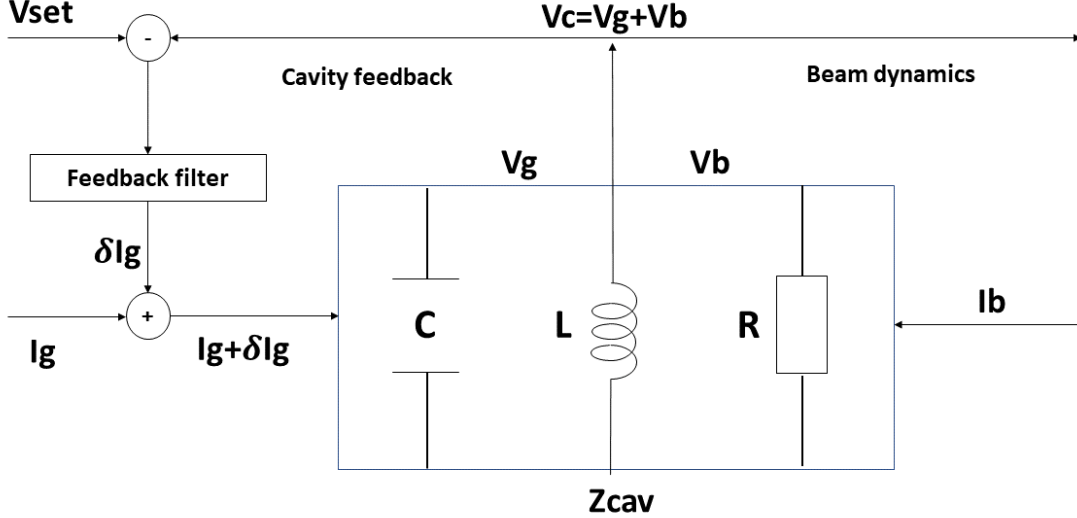


FIG. 3. Interaction between generator dynamics, beam dynamics and RF feedback.

This procedure repeats on a turn-by-turn basis.

One last thing to emphasize, the above discussion assumes a zero bunch length. This approximation is not appropriate for a bunch with a finite length. In that case, the bunch can be cut into different bins in the time sequence, thereafter, the bins of each bunch can be treated as zero-length micro-bunches, which pass through the cavities one after another. Then the Eq. 26, Eq. 29 and Eq. 30 are still available.

4. CODE IMPLEMENTATION AND BENCHMARKS

We chose the H6BA lattice of the PETRA-IV storage ring [15] to demonstrate the capability of CETASim. The project will adopt the active 3rd harmonic rf system to lengthen the bunches, reducing the particle densities at the core. The ideal bunch lengthening condition requires $\Re(\tilde{V}_c(\tau = 0)) = U_0/e$ to compensate the radiation loss U_0 , $\Re(\tilde{V}'_c(\tau = 0)) = \Re(\tilde{V}''(\tau = 0)) = 0$ to have a flat RF potential. The broadband impedance comprises the RW impedance and the geometric impedance. The RW impedance is created by the resistive chambers of the IDs, as well as the rest of the ring. The geometrical impedances are due to the elements in the ring such as BPMs, Bellows, Flanges, etc. The program

TABLE I. Nominal Lattice parameters of PETRA-IV H6BA lattice.

Parameters	units	symbol	DW Closed	DW Open
Energy	GeV	E	6	6
Circumference	m	C	2304	2304
Natural Emittance	pm	ϵ_0	20	43
Emittance Ratio		κ	0.1	0.1
Tunes		ν_x/ν_y	135.18/86.27	135.18/86.23
Momentum Compact Factor		α_c	3.33×10^{-5}	3.33×10^{-5}
Damping Time	ms	τ_x	17.76	39.23
Damping Time	ms	τ_y	22.14	69.63
Damping Time	ms	τ_s	12.62	56.84
Natural Energy Spread	rad	σ_E	8.9×10^{-4}	7.37×10^{-4}
Natural Bunch Length	mm	σ_s	2.3	1.794
Energy Loss	MeV	U_0	4.166	1.423
Main Cavity Voltage	MV	$V_{c,1}$	8	8
Main Cavity Harmonics		h	3840	3840

ImpedanceWake2D [16] is used to compute the resistive wall impedance. GdfidL computes the geometric wake potentials [17], where a 1 mm long Gaussian bunch is used as the driving bunch. We processed the wake potential of the bunched beam to get the impedance data via FFT divided by the bunch spectrum. Fig. 4 shows the wake potential in the longitudinal, horizontal, and vertical direction of the 1 mm leading electron Gaussian bunch and its corresponding impedance of Green-function wake. Here, the transverse wake potential and impedance are multiplied by the average betatron function $\langle\beta\rangle$ so that the units shown differ from conventional ones.

4.1 Zero current beam equilibrium state

Firstly, we would like to show how the radiation damping and the quantum excitation affect the beam in CETASim. We prepare one bunch with an initial Gaussian distribution both in the longitudinal and transverse phase space. 10^4 macro-particles are generated. The

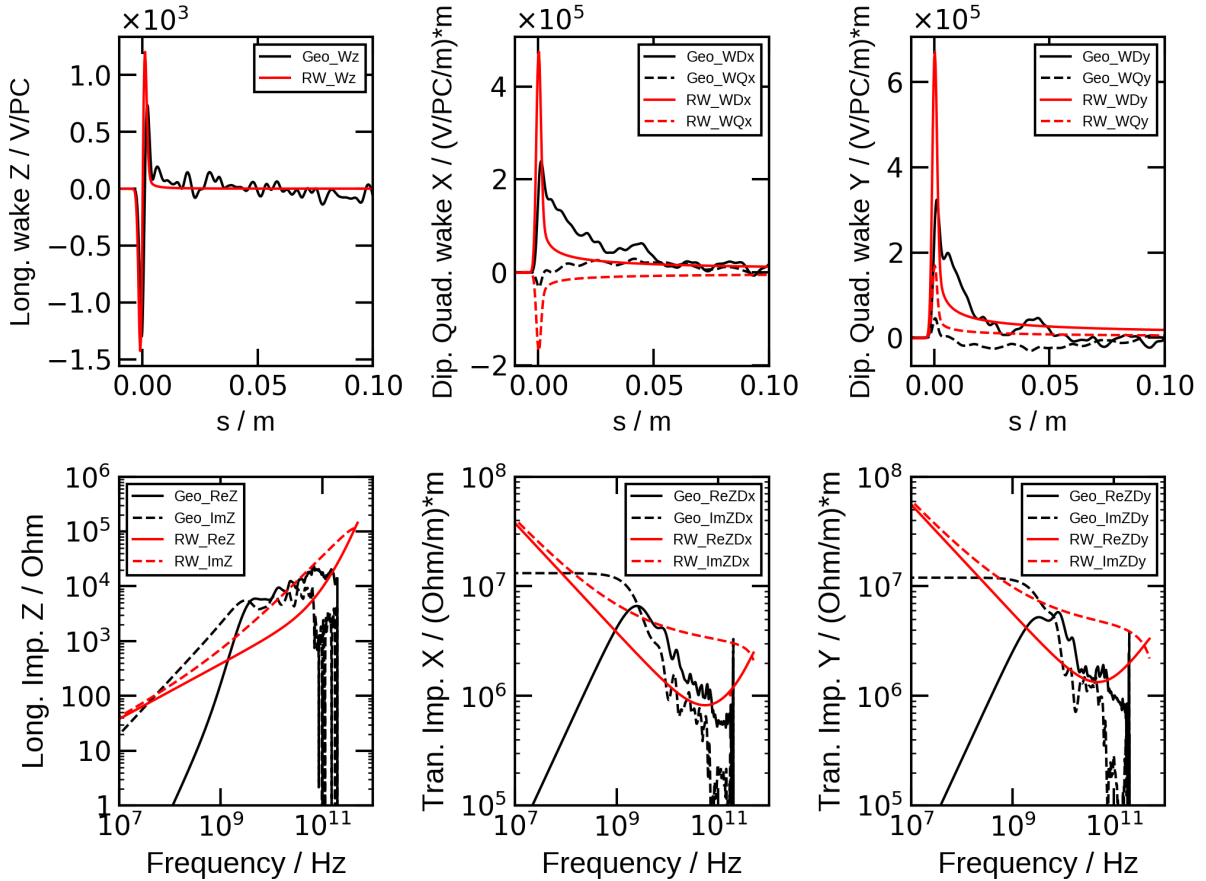


FIG. 4. Above: wakefield of a 1 mm leading electron Gaussian bunch from the geometrical impedance and the resistive wall impedance. Bottom: the geometrical impedance and the resistive wall impedance. From left to right, figures correspond to the longitudinal, horizontal and vertical directions respectively. The quadrupole impedance is not plotted here.

initial transverse bunch emittance is set as $\epsilon_{x,0} = \epsilon_{y,0} = 10$ pm, and the initial energy spread and bunch length are set as $\sigma_{E,0} = 8.9 \times 10^{-4}$ rad, $\sigma_{z,0} = 5.3 \times 10^{-3}$ m. The emittance ratio κ in the transverse plane and the radiation damping times shown in Tab. I are adopted in simulation. Fig. 5 shows how the bunch length, energy spread and the transverse emittance evolve as a function of tracking turns. The beam evolves to the natural equilibrium state as expected.

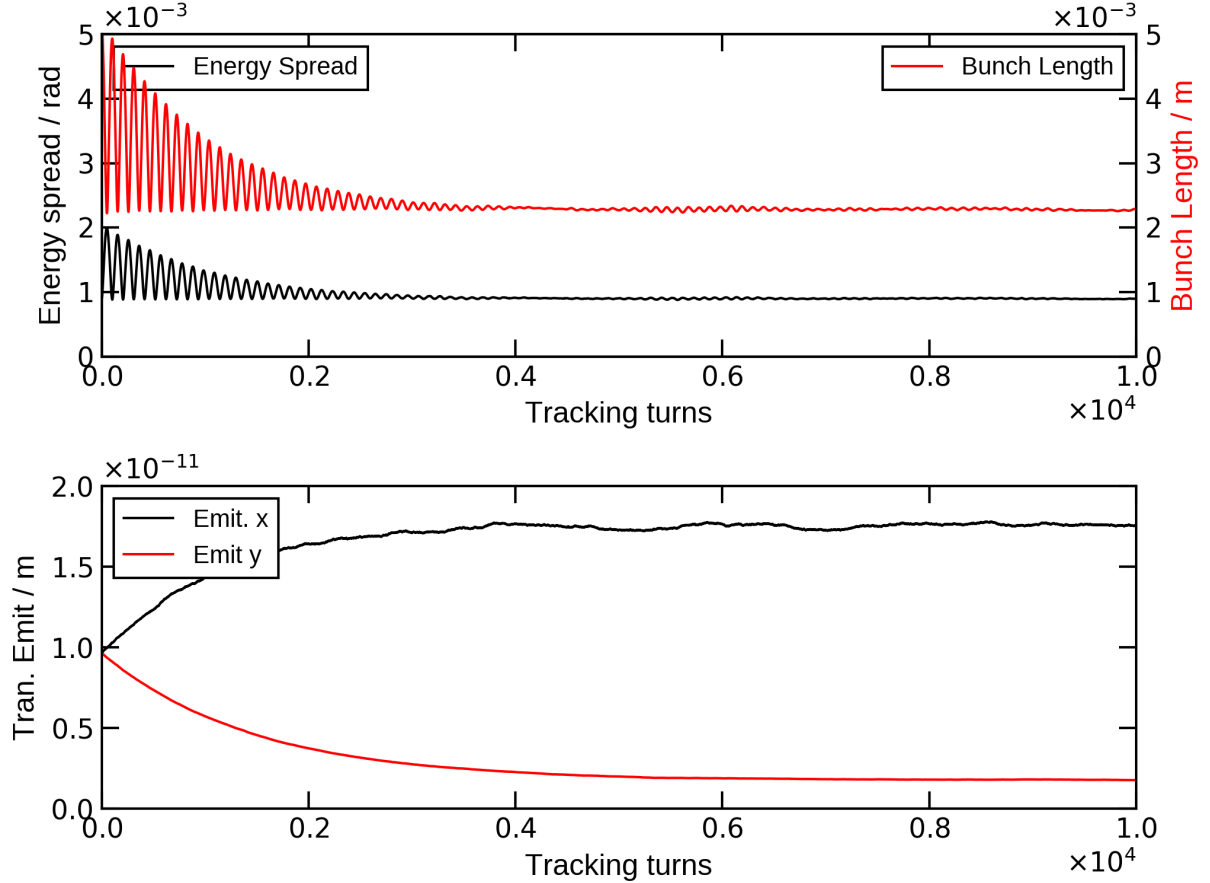


FIG. 5. Bunch energy spread, bunch length (top) and transverse beam emittance (bottom) as a function of tracking turns. The beam evolve to the natural equilibrium state as expected.

4.2 Single bunch effect

With the broadband impedance shown in Fig. 4, we perform a study of the single-bunch effects. The longitudinal impedance leads to a potential well distortion and bunch lengthening. Once the single bunch current increases further and the longitudinal microwave instability threshold is reached, the energy spread starts to increase as well. In below, we show two scenarios studied by CETASim: the main cavity only and the main cavity together with a 3rd harmonic cavity. In both scenarios, the beam loading effect is not included. In the double RF case, the generator voltage and phase are set to maintain the ideal bunch lengthening condition. Fig. 6 shows the single bunch length and energy spread as a function of the single bunch current. In each sub-figure, two groups of curves are given. The red ones are from CETASim and the black ones are from Elegant. The bunch length given by

CETASim agrees well with results given by Elegant. Noticeably, there are discrepancies in the energy spread when the single bunch current is above the longitudinal microwave instability threshold which is usually out of practical interest.

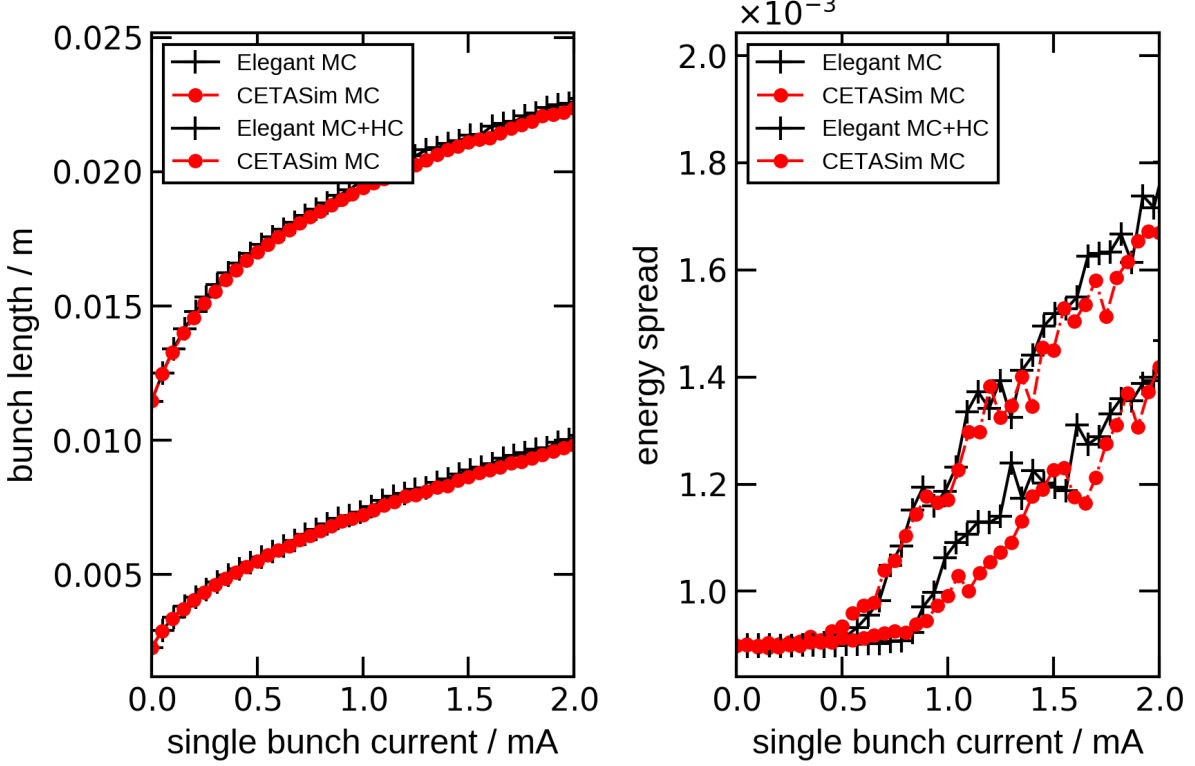


FIG. 6. Single bunch length (left), energy spread (right) as function of single bunch current. Results from CETASim and Elegant show very good agreements.

In the transverse plane, the impedance leads to the Transverse Mode Coupling Instability (TMCI) and head-tail instabilities. The azimuthal modes shift as the single bunch current increases. At a certain point, these azimuthal modes collide and merge, the beam becomes unstable. If there only exists the dipole impedance, the mode coupling condition can be found by Sacherer's method [6]. Considering the dipole impedance effect as a perturbation and decomposing the longitudinal phase space by the Laguerre polynomials, a set of Sacherer integral equations can be established, by solving which the beam threshold due to mode merge conditions can be found analytically. As a benchmark study, we set simulation with zero chromaticity and include the vertical dipole impedance only. The comparison of the azimuthal mode frequency shift between CETASim tracking and the Vlasov solver is shown

in Fig. 7. The results of modes' frequency shifts agree well.

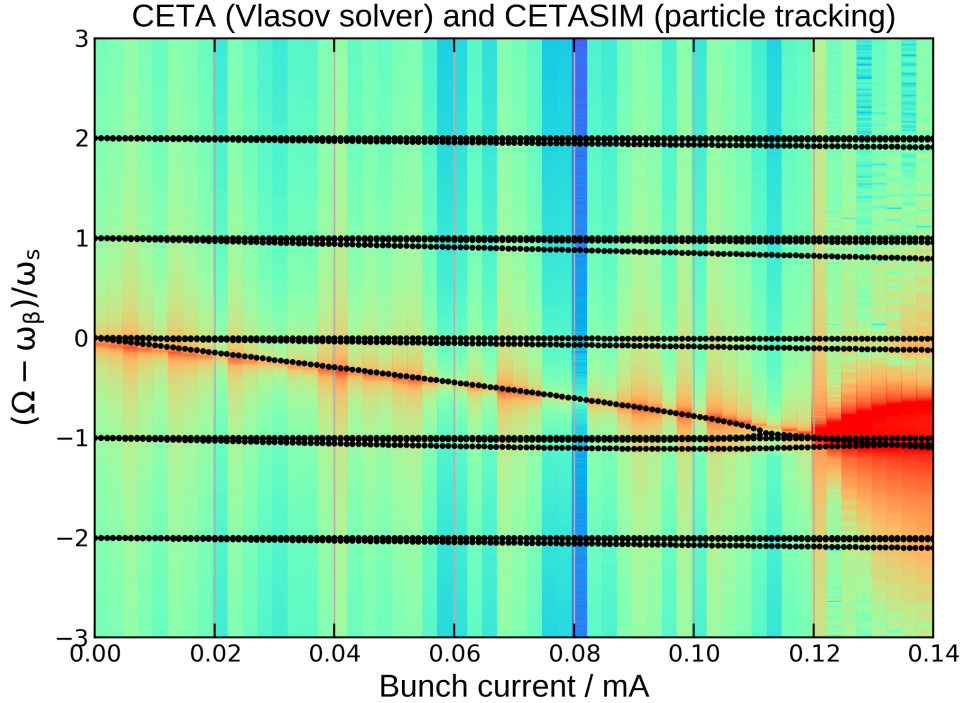


FIG. 7. Comparison of the TMCI threshold from Vlasov solver (black dots) and CETASim (contours). In CETASim tracking, only the vertical dipole impedance is included.

One way to increase the transverse single-bunch current limit is to set a non-zero chromaticity ξ . The chromaticity introduces a head-tail phase advance and shift the mode spectrum by $\omega_\xi = \xi f_0 / \eta$, where η is the lattice slip factor and f_0 is the nominal revolution frequency. Fig. 8 shows the single bunch current limit as a function of chromaticity without and with 3rd harmonic cavity. The transverse dipole, quadrupole impedance, and longitudinal impedance are all taken into account in the simulation. The threshold current is defined as the lowest bunch current, which leads to a non 100% transmission during the tracking, where an elliptical chamber with a radius (15, 10) mm is applied as the particle loss criteria. The particle loss occurs only in the vertical direction. The results from Elegant and CETASim show a good agreement.

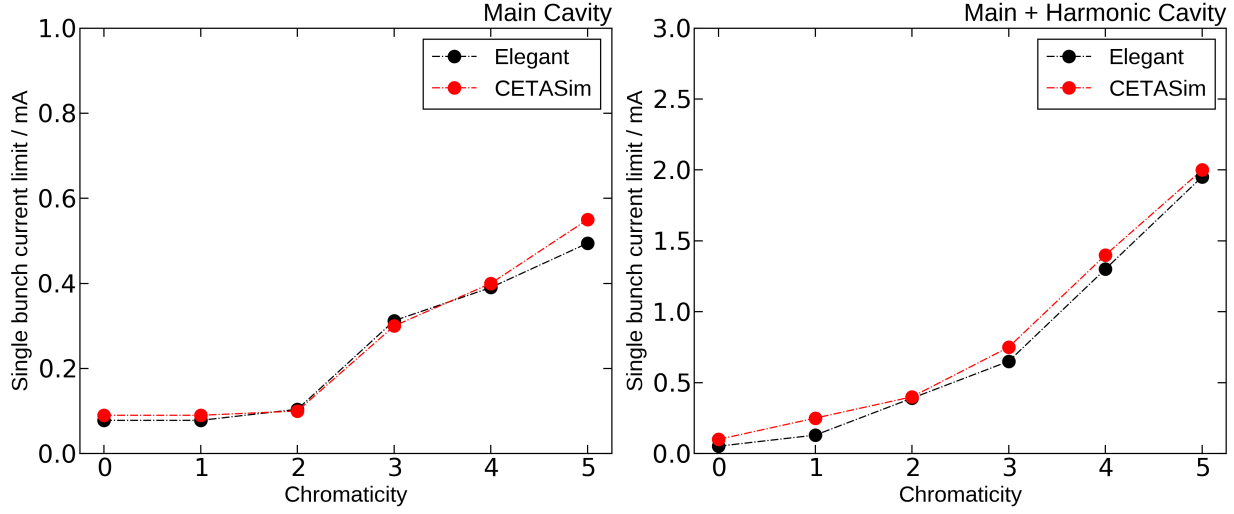


FIG. 8. The single bunch current threshold as a function of chromaticity without (left) and with (right) the 3rd harmonic cavity. Results from CETASim and Elegant show a good agreement.

4.3 Coupled-bunch instability due to the long-range wakes

In general, if the impedance is known and the filling pattern of the ring is uniform, the coupled bunch mode frequency shift and growth rate can be found by,

$$\begin{aligned} (\Omega^\mu - \omega_\beta)_\perp &= -i \frac{MNr_0c}{2\gamma T_0^2 \omega_\beta} \sum_{p=-\infty}^{\infty} Z_1^\perp [\omega_\beta + (pM + \mu)\omega_0] \\ (\Omega^\mu - \omega_s)_\parallel &= i \frac{MNr_0\eta}{2\gamma T_0^2 \omega_s} \sum_{p=-\infty}^{\infty} (\omega_s + pM\omega_0 + \mu\omega_0) Z_0^\parallel [\omega_s + pM\omega_0 + \mu\omega_0] \end{aligned} \quad (32)$$

where M is the number of equal spaced bunch number, N is the electron particle number per bunch, μ is the coupled bunch mode index varying from 0 to $M-1$, ω_β and ω_s are the transverse and longitudinal oscillation angular frequency respectively, σ_t is the bunch length. In particle tracking studies, the coupled bunch mode can be reconstructed when the bunch-by-bunch and turn-by-turn data is available. Take the horizontal plane for example, the coupled bunch mode can be obtained from the Fourier spectrum of the one-turn complex signal z_μ at certain BPM

$$z_\mu = \left(\frac{x_\mu}{\sqrt{\beta_x}} - i(\sqrt{\beta_x} p_{x,\mu} + \frac{\alpha_x}{\sqrt{\beta_x}} x_\mu) \right) e^{-i \frac{2\pi\nu_x(\mu-1)}{M}}, \quad (33)$$

where β_x and α_x are the twiss parameters at the BPM. The growth rate of the μ th mode can be obtained by an exponential fitting of the μ th mode spectrum amplitude as a function of time.

However, in a real machine, what can be measured at the BPMs is limited to the position information only. In CETASim, we also supply another approach to get the coupled bunch instability growth rate by following the process of drive-damp experiments [18]. A driver element in CETASim excites the beam with a given kick strength in the frequency f_μ by which the μ th coupled bunch mode can be excited. Then the signal

$$\tilde{S}_n^\mu = \sum_{m=0}^M \tilde{s}_{n,m}^\mu = \sum_{m=0}^M x_{n,m} \exp(-i2\pi f_\mu h T_{rf}/M), \quad (34)$$

is recorded turn by turn. The growth rate of the excited μ th mode excited can be found by an exponent fitting of $|\tilde{S}_n^\mu|$. Then, one can reconstruct the full picture of the coupled-bunch mode by scanning the driving frequency f_μ .

As discussed in Section 3, in CETASim, there are two analytical models to generate the long-rang wakes, the RLC model and the RW model. In below, two examples are given for the transverse coupled bunch effect study. The first one is transverse impedance given by a RLC model with the parameters $R_s = 5 \times 10^9 \text{ ohm/m}^2$, $Q = 1 \times 10^{-3}$ and $\omega_r = 2\pi \times 4.996 \times 10^9 \text{ 1/s}$. The second one is a simplified resistive wall impedance of PETRA-IV storage ring, where the vacuum chamber is grouped into 4 types of sections as shown in Tab. II. The characteristic distance z_0 of this four sections are in the order of $1. \times 10^{-5} \text{ m}$, which is much smaller than the RF bucket distance $cT_{rf} = 0.6 \text{ m}$, so that Eq. 14 applied in CETASim is still a good approximation. In the simulation, the ring is filled uniformly by 80 bunches and each bunch has 1 mA current. The long-range wakes are truncated at 20 turns. The synchrotron radiation damping is turned off. In Fig. 9, we give the results of the coupled mode growth rate from CETASim tracking and analytical predictions of these two cases. 'Ideal' and 'Prediction' legend indicates the results are obtained from tracking and Eq. 32 respectively. The results obtained from tracking show very good agreements with predictions for both RLC and RW impedance.

Figure 10 represents the coupled bunch modes reconstructed from the drive-damp method. The driving strength of the exciter is $0.2 \mu\text{rad}$ and the excitation time is limited to the first 300 turns. The next 700 turns bunch-by-bunch data are used for coupled bunch mode growth rate calculation. The other simulation conditions are the same as those used in Fig. 9, except the radiation damping is turned on. For a better comparison, the results obtained from Eq. 33 ('Ideal') are also plotted. Both methods give the same coupled bunch growth rate. Compared to results in Fig. 9, the growth rates are decreased by the radiation

TABLE II. Simplified resistive wall sections in PETRA-IV.

section	number	length / m	gaps / mm	β_x / m	β_x / m	conductivity σ / $\Omega^{-1}m^{-1}$	z_0 / m
5 mm ID	4	5	5	3.14	3.14	2.5×10^7	1.74×10^{-5}
6 mm ID	17	5	6	3.14	3.14	2.5×10^7	1.97×10^{-5}
7 mm ID	5	10	7	6.08	6.08	2.5×10^7	2.18×10^{-5}
ring	1	2149	10	2.71	4.25	5.9×10^7	2.08×10^{-5}

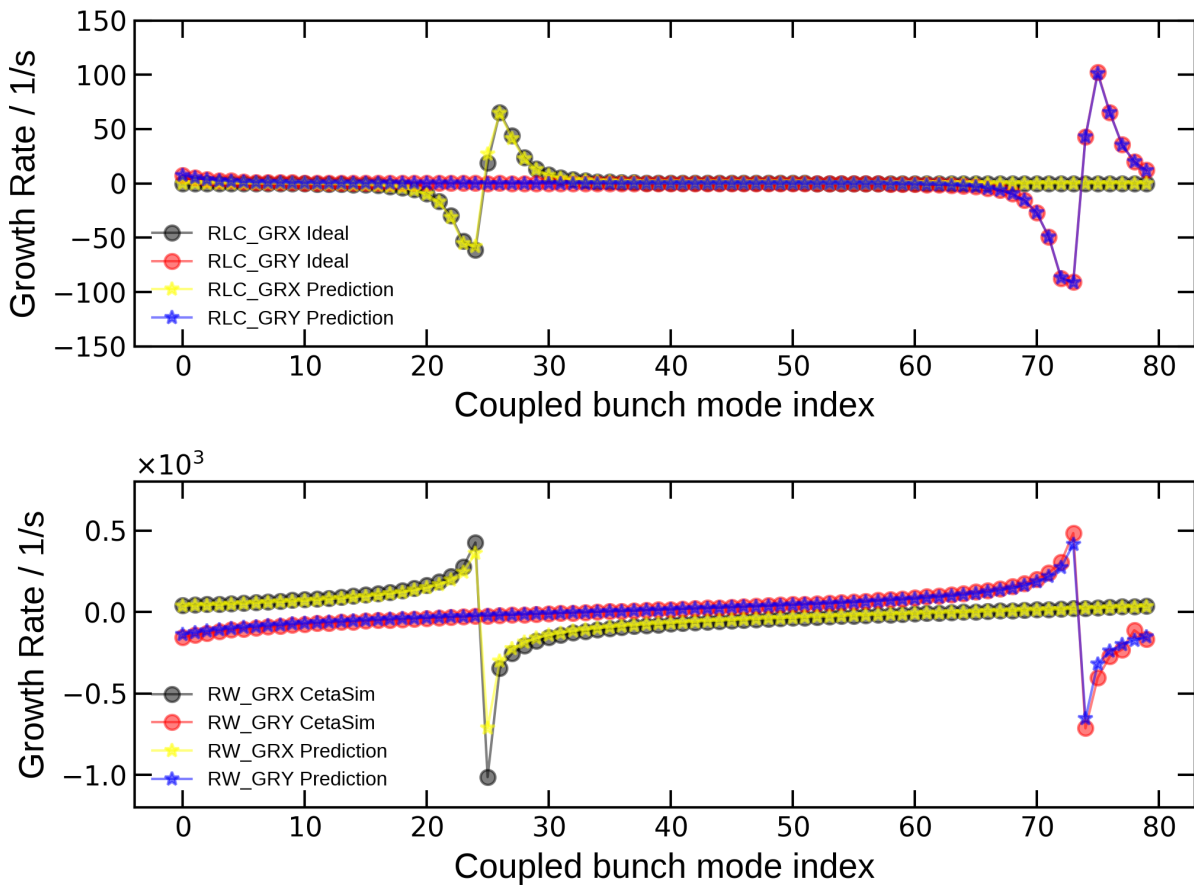


FIG. 9. Growth rate of the transverse coupled bunch modes from RLC (top) and RW (bottom) wakes. The RLC parameters are $R_s = 5. \times 10^9 \text{ ohm/m}^2$, $Q = 1. \times 10^3$ and $\omega_r = 2\pi \times 4.996 \times 10^9 \text{ 1/s}$. The parameters to get the RW wakes are shown in Tab. II. The ring is filled uniformly by 80 bunches and each bunch current is 1 mA. The long-range wakes last 20 turns and the SR damping is turned off. 'Ideal' and 'Prediction' indicate the results are obtained from Eq. 33 and Eq. 32 respectively.

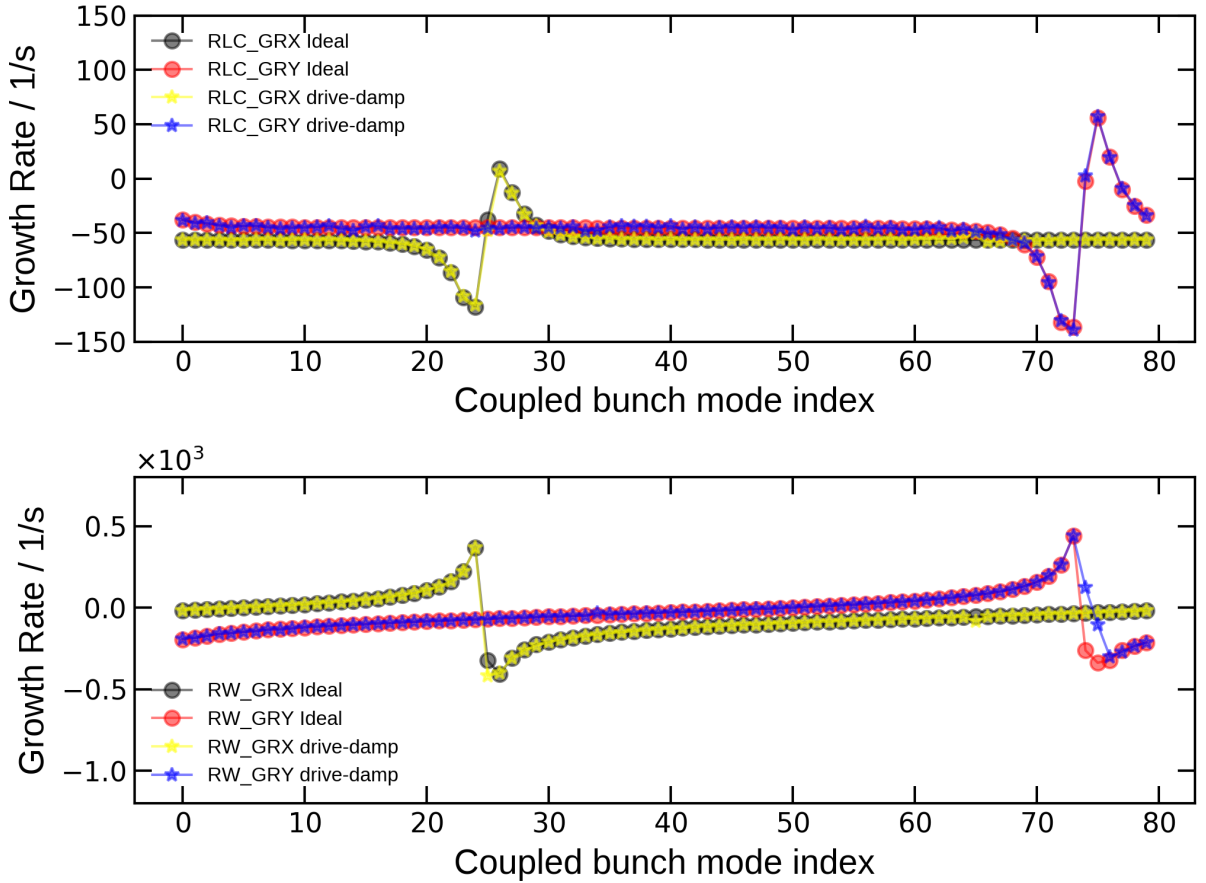


FIG. 10. Growth rate of the transverse coupled bunch modes from RLC (top) and RW (bottom) wakes. The long-range wakes last 20 turns and the synchrotron radiation damping is turned on. 'Drive-damp' indicates the results are obtained from Eq. 34.

damping as expected. The drive-damp method is one of the most important approaches if one wants to reconstruct the narrow-band impedance information from the real experimental turn-by-turn data.

Finally, in the longitudinal direction, the tracking studies with the longitudinal long-range wakes can be set up similarly. However, it is not trivial to make the longitudinal coupled bunch mode growth rate comparable with the analytical prediction because the RF phase particle experiences in the cavities is shifted by the longitudinal wakes.

TABLE III. RF parameters of PETRA-IV storage ring.

Parameter	Symbol	Main RF ($n = 1$)	Harmonic RF ($n = 3$)
RF Freq. (Hz)	$f_{rf,n}$	4.996×10^8	1.499×10^9
Ref. Voltage (V)	$V_{c,n}$	8×10^6	2.223×10^6
Synchronous Phase (Rad)	ϕ_n	2.516	-0.236
Detuning Freq. (Hz)	Δf_n	-27.9×10^3	277.6×10^4
Coupling Factor	β_n	3.0	5.3
Shunt Impedance	$R_{s,n}$	81.6×10^6	$36. \times 10^6$
Quality Factor	$Q_{0,n}$	29600	17000
Gen. Curr. Amp. (Amp.)	$Abs(\tilde{\mathbf{I}}_g)$	0.626	0.294
Gen. Curr. Phase (Rad)	$Arg(\tilde{\mathbf{I}}_g)$	0.945	-1.813
Total Generator Power (W)	$P_{g,n}$	1.34×10^6	7.40×10^4
Total Reflected Power (W)	$P_{r,n}$	4.98×10^3	1.09×10^5

4.4 Transient beam loading effect

Transient beam loading brings two effects: the longitudinal coupled bunch instability and an unexpected bunch lengthening. In CETASim, the coupled bunch instability can be turned off by ignoring the distance variation among bunches. In that case, the tracking results always converge to an equilibrium state. Meanwhile, if the tracking is set up with only one macro-particle per bunch, according to the phase and voltage this particle samples, the bunch profile can be found analytically by

$$\rho(z) = \rho_0 \exp\left(-\frac{1}{2\pi h f_0 \alpha_c \delta^2} H_1(z)\right),$$

$$H_1(z) = \frac{\omega_0 e}{2\pi \beta^2 E} \frac{2\pi h f_0}{\beta c} (Re \sum_n \int_0^z \tilde{\mathbf{V}}_{c,n}(z') dz' + \int_0^z \int_{z''}^{\infty} e \rho(z') W'_0(z'' - z') dz' dz''). \quad (35)$$

$H_1(z)$ is the Hamiltonian composed by terms due to the RF potential and the short-range wakes [6]. If multi-particles are set per bunch, then the bunch profile can be obtained by binning the distribution along the longitudinal in real space. Tab. III gives the RF parameters of the main cavity and the 3rd harmonic systems used in PETRA-IV. The cavities are de-tuned to the 'optimized' condition to have the lowest power consumption. The filling pattern of the ring is set as $h = 3840 = 80 * (20 * (1+1) + 8)$. There exist 80 bunch

trains and in each bunch train, every bucket is occupied by the electron beam except the last 8 buckets. The total beam current is 200 mA. In below, we give the simulation results by turning off the longitudinal coupled bunch instability. Fig. 11 shows how the amplitude and phase of the beam induced voltage \tilde{V}_b , generator voltage \tilde{V}_g and cavity voltage \tilde{V}_c are built up as functions of turns. With the optimum de-tuning condition, the generator voltage driven by \tilde{I}_g is simulated from the 0th turn, whereas the beam induced voltage driven by \tilde{I}_b is simulated from the 5th turn. Finally, the cavity voltage \tilde{V}_c beam supposed to sample converges to the designed values as expected.

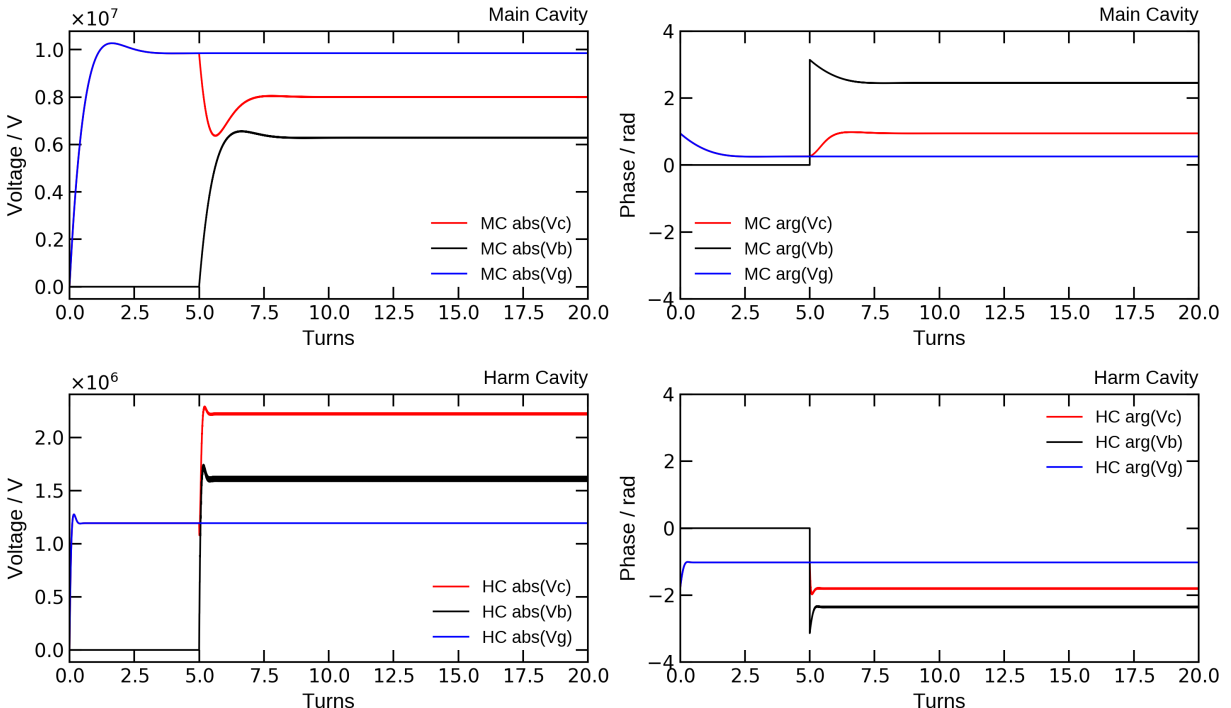


FIG. 11. The amplitude (left) and phase (right) of beam induced voltage \tilde{V}_b , generator voltage \tilde{V}_g and cavity voltage \tilde{V}_c on the main cavity (top) and harmonic cavity (bottom) as function of turns. The beam are injected to the ring from the 5th turn.

Figure 12 shows the simulation results by setting one macro-particle per bunch. The sub-figures on the left and in the middle depict the cavity voltage and phase sampled by the bunches in the first 4 bunch trains. The sub-figures on the right show the bunch center shift and bunch length variation. Clearly, the periodic filling pattern leads to a periodical voltage sampling, which further reduces to a periodical bunch center offset and bunch lengthening effect. The bunch profile obtained from Eq. 35 as function of RF bucket index can be found

in Fig. 13.

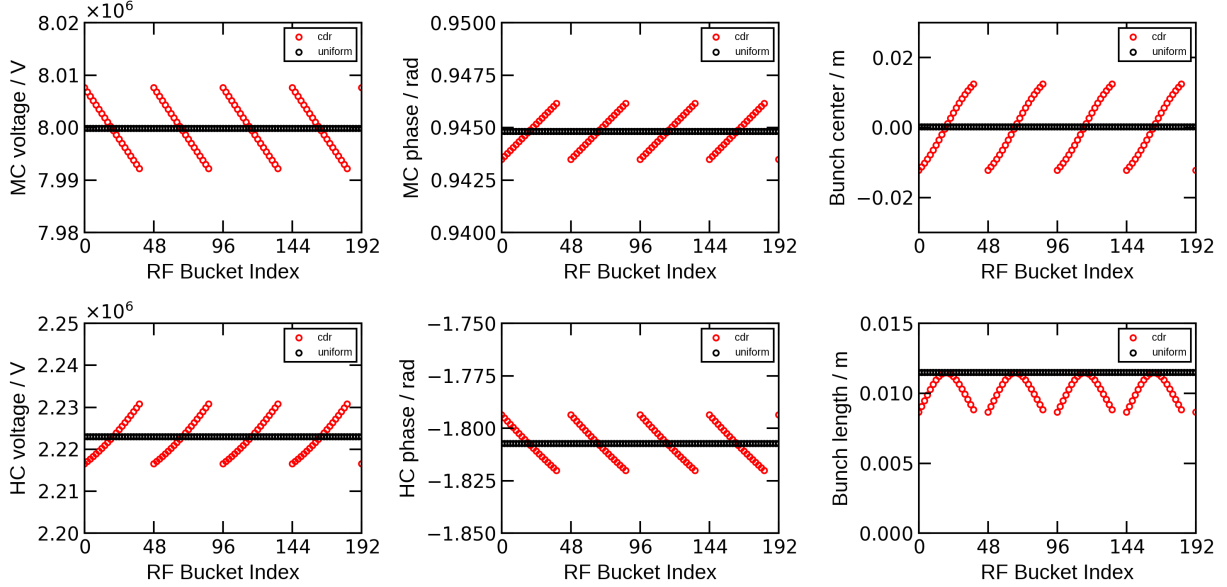


FIG. 12. The cavity voltage $Abs(\tilde{\mathbf{V}}_c)$ (left), cavity phase $Arg(\tilde{\mathbf{V}}_c)$ (middle) bunch sampled at the main cavity (top) and harmonic cavity (below); the right column gives the bunch center and bunch length. The total beam current is 200 mA.

We would like to introduce a simple equation [19], which can be used to estimate the cavity phase modulation $\delta\phi_{max}$ due to the empty gaps δt in a bunch train,

$$\delta\phi_{max,n} = \frac{1}{2} \frac{R_{s,n}}{Q_{0,n}} \frac{2\pi f_{rf,n}}{V_{c,n}} I_{DC} \delta t. \quad (36)$$

With the filling pattern $h = 3840 = 80 * (20 * (1 + 1) + 8)$, Eq. 36 gives the peak-to-peak phase variation around 0.0037 and 0.029 rad for the main cavity and harmonic cavity, which are rather good estimation compared to the results from CETASim simulation shown in Fig. 12.

Simulation with macro-particles per bunch can be done similarly. Set 3000 macro-particles in each bunch and turn off the longitudinal coupled bunch instability in tracking, we give the results of bunch center shift and bunch length variation after 3000 turns in Fig. 14. The bunch profiles are given in Fig. 15. Compared with the results in Fig. 12 and Fig. 13, single particle and multi-particle tracking gives the same results as expected.

As discussed in previous section, the growth rate of the longitudinal coupled bunch mode can be estimated by Eq. 32. If the synchrotron radiation damping can not suppress the

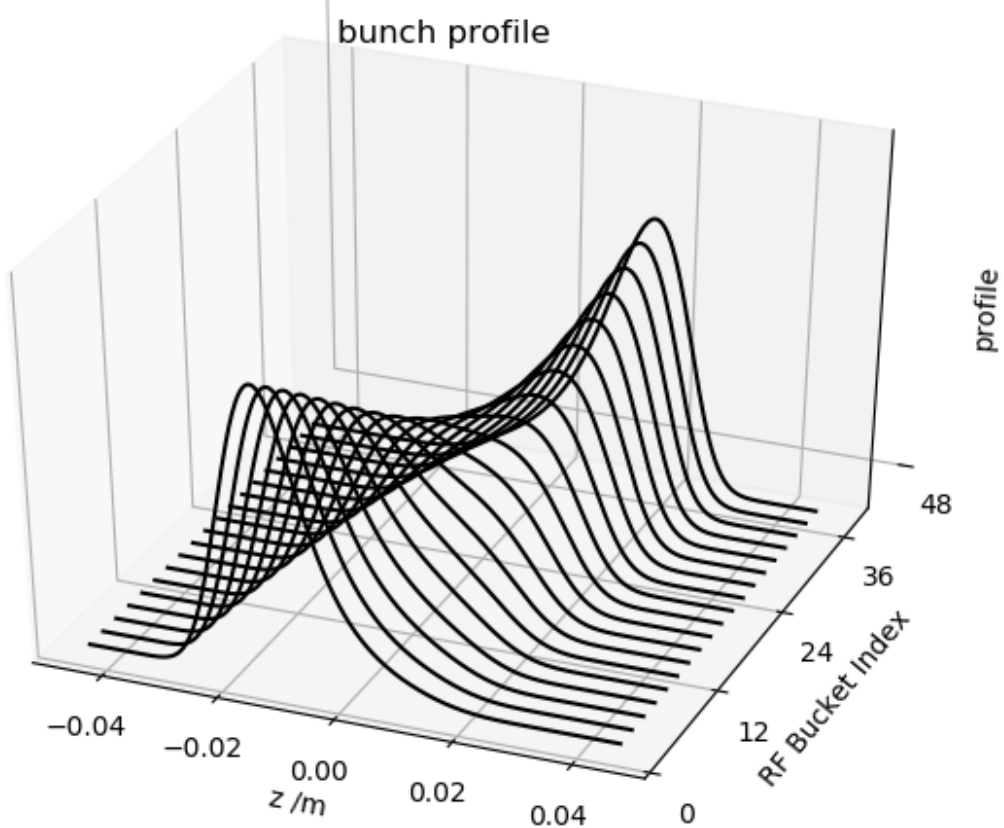


FIG. 13. Bunch profile as a function of RF bucket index in the first 4 bunch trains. The profile are obtained from Eq. 35.

instability, the low-level RF feedback, RF feedforward, or the longitudinal bunch-by-bunch feedback have to be applied to stabilize the beam. Here we briefly introduce the stabilization mechanism when a low-level RF feedback is applied. From the control theory, when the low-level RF feedback is included in the control loop, the impedance sampled by the beam is modified by

$$Z_{cl}(\omega) = \frac{Z(\omega)}{1 + \exp(-i\omega\tau)G(\omega)Z(\omega)\exp(i\phi)}, \quad (37)$$

where τ is the overall loop delay, ϕ is the loop phase adjusted and $G(\omega)$ is the gain factor. In Ref. [19], it is shown that the minimum value of the impedance beam can sample is

$$R_{min} = \frac{2}{\pi}\tau\frac{R_s}{Q}\omega_{rf}. \quad (38)$$

For a rough estimation, in the harmonic cavity of PETRA-IV, with a overall loop delay

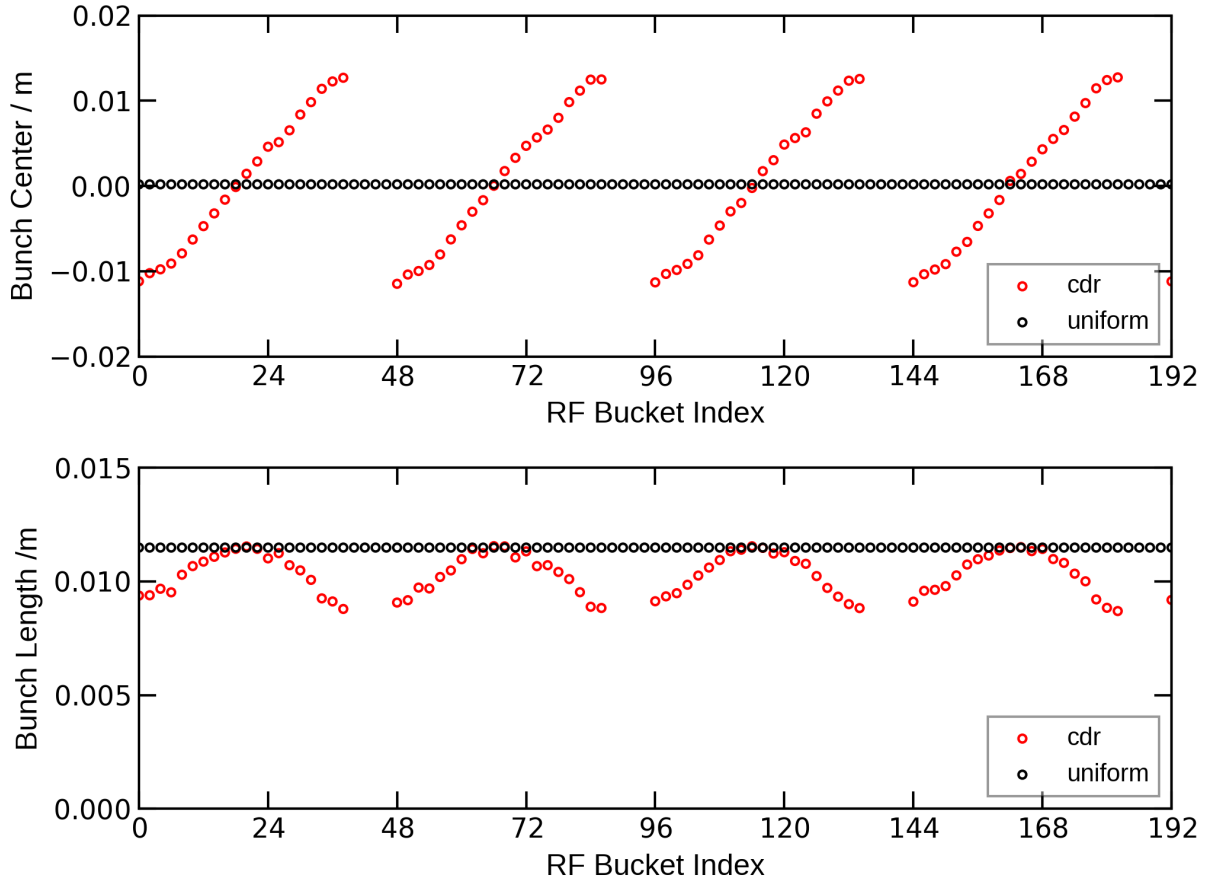


FIG. 14. Bunch center and bunch length variation of the first 4 bunch trains as function of RF bucket index. The results are obtained from multi-particle tracking and each bunch is composed of 3000 macro-particles.

$\tau = 150$ ns, the R_{min} would be decreased by a factor of 20, so that the coupled bunch growth rate due to the harmonic cavity would be significantly decreased.

In the following part, we show the benchmark between CETASim and Elegant of the transient beam loading simulation when the coupled bunch instability mechanism is turned on. To stabilize the beam, the shunt impedance of the main cavity and harmonic cavity are reduced by a factor of 2 and 20 respectively. Correspondingly, the cavity de-tuning frequency Δf_n are modified to $\Delta f_1 = -13.953$ kHz and $\Delta f_3 = 13.882$ kHz to maintain the "optimized" de-tuning condition. The beam filling pattern is set as $h = 3840 = 2 * (100 * (1 + 9) + 920)$ which means there are 2 bunch trains and each bunch train includes 100 bunches. The total beam current is set as 200 mA as well. Fig. 16 shows the comparison of the beam induced

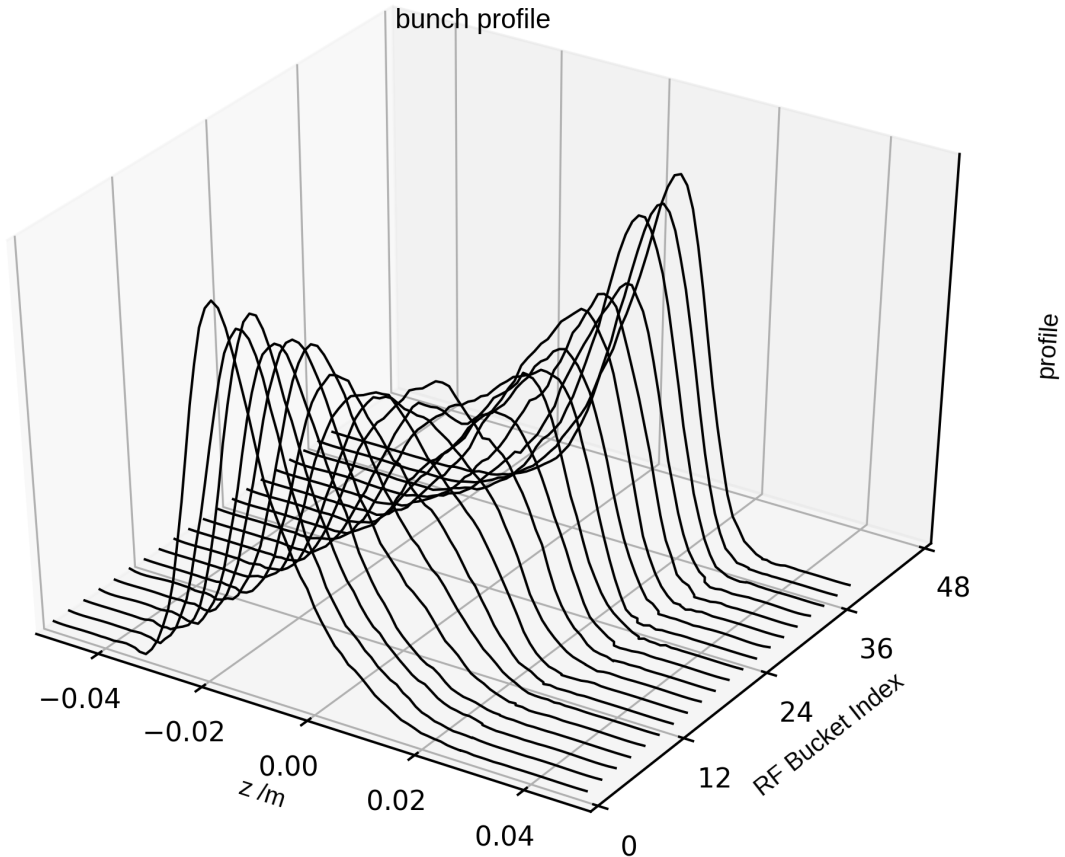


FIG. 15. Bunch profiles as function of RF bucket index in the first bunch train. The results are obtained from multi-particle tracking and each bunch is composed of 3000 macro-particles.

voltage and generator voltage on the bunch center at the 1000th turn. Results from Elegant and CETASim agree well.

4.5 Beam-ion effect

As shown in Eq. 21, ions with a mass number larger than A_c can be trapped in rings. If the oscillation of the trapped ions is confined within the beam pipe, a beam-ion instability might occur. Roughly speaking, with a high bunch charge, ions are over-focused and get lost within the gaps between bunches. With a low bunch charge, more ions can be trapped. However, if the bunch charge is too small, only a few ions can be ionized, leading to a weak beam-ion effect as well [20]. In this sense, we expect the beam-ion effect to be of interest in the medium bunch charge region. In CETASim, the ion motion is limited in the

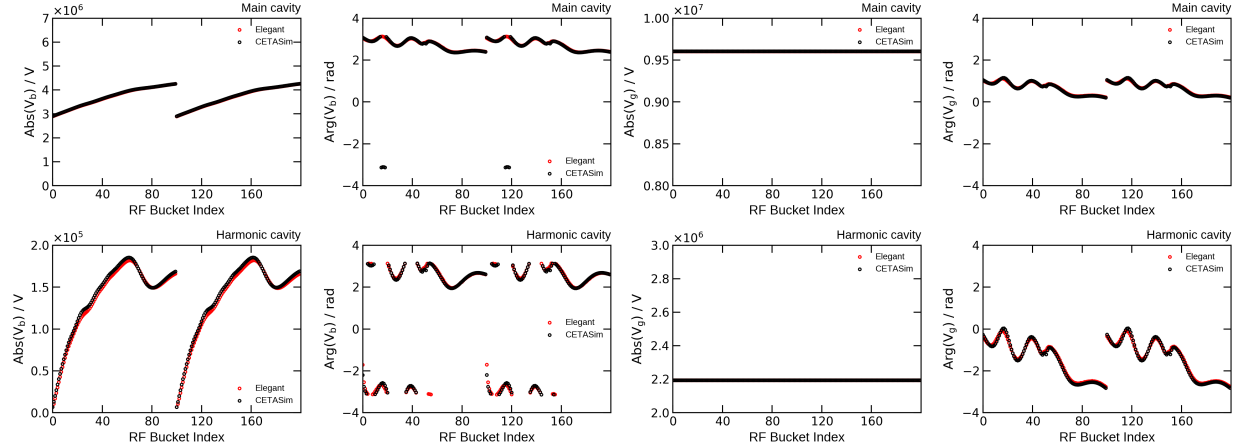


FIG. 16. The amplitude and phase of the beam induced voltage \tilde{V}_b and generator voltage \tilde{V}_g each bunch sampled at the main cavity (top) and the harmonic cavity (bottom) after 1000 turn tracking from Elegant and CETASim.

transverse direction. CETASim supplies several parameters to act as comprise of simulation speed and accuracy, such as the number of macro-ions generated per collision, the transverse range beyond which the ions are cleaned, the number of beam-ion interactions per turn, etc. Below, we give two examples of the beam-ion effect simulation in PETRA-IV storage ring, single and multi-ion species. The filling pattern is set as the brightness mode operation scheme, $h = 3840 = 80 * (20 * (1 + 1) + 8)$, and the bunch charges are identical among the 1600 bunches. It is assumed that the total gas pressure is 1 $n\text{Tor}$ and the gas temperature is 300 K . We set one beam-ion interaction point in one turn and take the average betatron functions to get the one-turn transfer matrix. In the simulation, one electron bunch is represented by one macro-electron particle. The electron bunch position is initialized on the axis. Ions are cleaned when their transverse distances reference to the ideal orbit are larger than 10 times the maximum effective beam size $\text{abs}(\mathbf{X}_i) > 10 * (\text{abs}(\langle \mathbf{x} \rangle) + \sigma_x)$.

Set residual gas including CO only, Fig. 17 shows the equilibrium transverse ion CO^+ profile after 10 K turns tracking when the total beam current is 5 mA. For each beam-ion collision, 50 macro-ions are generated. Clearly, the ion density profile does not follow a Gaussian shape as pointed out in Ref. [21]. Fig. 18 (left) gives the square root of the maximum vertical action $\sqrt{J_y}$ among 1600 bunches as a function of tracking turns. The

action $\sqrt{J_y}$ is defined as

$$J_y = \frac{1}{2} \left(\frac{1 + \alpha^2}{\beta} y^2 + 2\alpha y p_y + \beta p_y^2 \right), \quad (39)$$

where α and β are the Twiss functions at the beam-ion interaction points. The square root of the bunch action $\sqrt{J_y}$ increases firstly and then gets saturated gradually to a value around $\sqrt{40\epsilon_y}$. Fig. 18 (middle) gives the growth rate of $\sqrt{J_y}$ as a function of the total beam current. The growth rate is obtained by an exponential fitting of $\sqrt{J_y}$ data selected in between $(\sqrt{0.1\epsilon_y}, \sqrt{3\epsilon_y})$, indicating that the beam-ion effect is more sever in the median beam current region. Figure 18 (right) shows the final accumulated CO^+ charge as function of the beam current. Again, at the median beam current region, more ions could be accumulated.

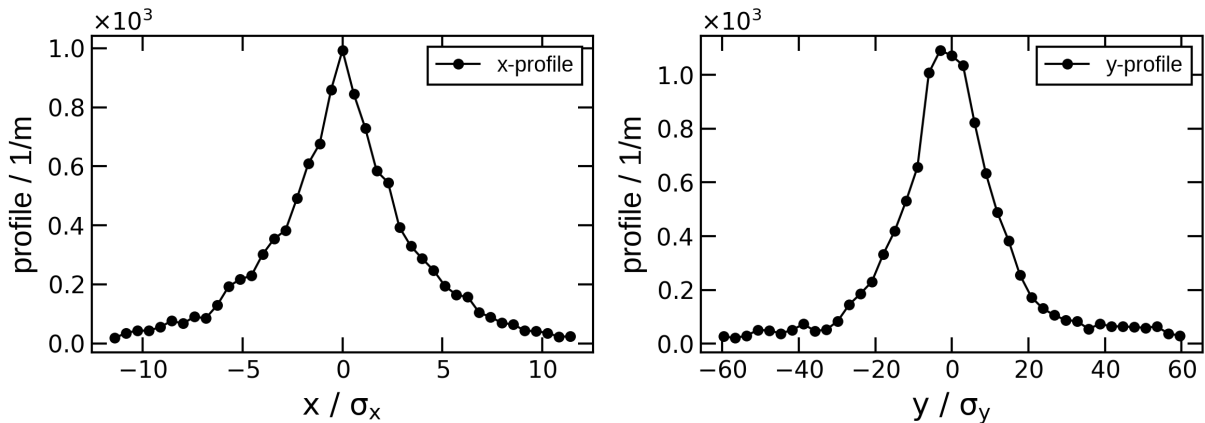


FIG. 17. The equilibrium ionized CO^+ profile along x and y direction. The total beam current in simulation is set as 5 mA. Clearly, the profiles of the accumulated ion-cloud does not follow a Gaussian shape. The ion gas is composed of CO only.

In the second simulation, the initial gas composition is chosen identical to that in APS-U [15], where the residual gas is composed of H_2 , CH_4 , CO and CO_2 . The percentage of each gas is 0.43, 0.08, 0.36 and 0.13 respectively. Simulation results are shown in Fig. 19. Similar to the results obtained from the single-ion gas setting, the beam-ion effect is more severe in the median beam current region. The $\sqrt{J_y}$ saturates gradually to a value around $\sqrt{20\epsilon_y}$. The growth rate is reduced roughly by a factor of 2. The sub-figure on the right gives the ion charge accumulated finally after 10 K tuns tracking. Clearly, the higher the total beam current is, the less of the lighter ions can be trapped. The total accumulated ion charge decreased roughly by a factor of 2 as expected.

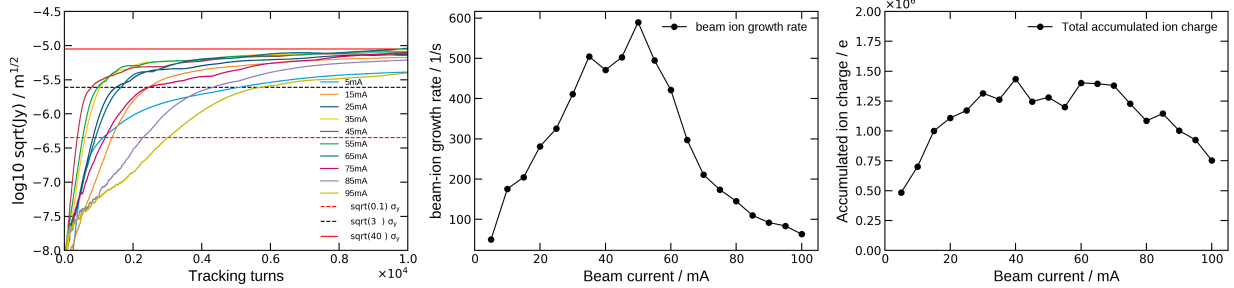


FIG. 18. Left: the square root of the maximum vertical action $\sqrt{J_y}$ among 1600 bunches as a function of tracking turns; Middle: beam ion growth rate as a function of the total beam current; Right: the final accumulated ion charge after 10 K turns tracking as a function of the total beam current. The ion gas is composed of CO only. The maximum bunch action $\sqrt{J_y}$ saturate to a value around $\sqrt{40\epsilon_y}$.

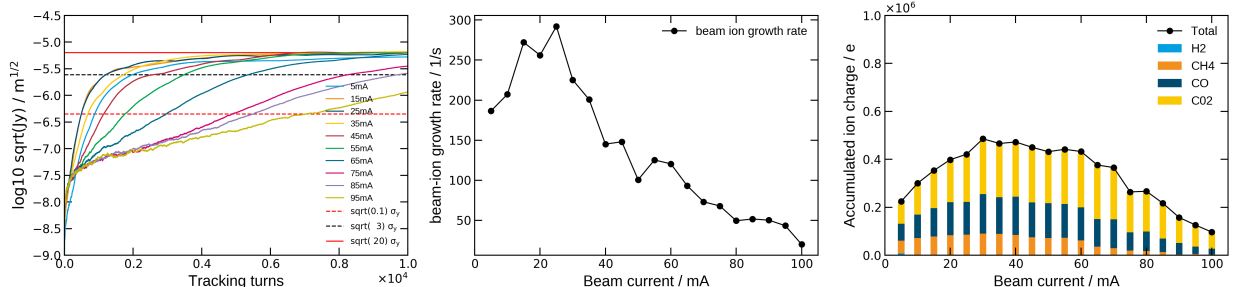


FIG. 19. Left: the square root of the maximum vertical action $\sqrt{J_y}$ among all bunches as a function of tracking turns; Middle: beam ion growth rate; Right: the final accumulated ion charge after 10 K turns tracking. The maximum bunch action $\sqrt{J_y}$ saturate to a value around $\sqrt{20\epsilon_y}$.

There are several things noticeable for the beam-ion study. Firstly, the beam-ion instability is usually not strong and is self-limited. This beam-ion instability can be handled by the normally used bunch-by-bunch feedback. Secondly, according to the $\sqrt{J_y}$ selected for growth rate fitting, the result would be different. In CETASim, the turn-by-turn data and bung-by-bunch data are available, which supplies detailed information for further analysis. Thirdly, the convergence of the simulations as different parameters settings, such as the number of beam-ion interaction points, the number of ions generated per beam-ion collision, the range to clean ions, etc, has to be studied beforehand. From our experience, cutting the ring into 10 sections usually gives a very good convergence of total ion charge accumulated in

simulation. Set 10 macro-ions per collision is good comprising between speed and accuracy. Set ion cleaning condition m as 10 ($\text{abs}(\mathbf{X}_i) > m * (\text{abs}(\langle \mathbf{x} \rangle) + \sigma_x)$) is usually not a bad choice. The last thing is about the incoherent effect. If one wants to simulate the bunch emittance growth instead of the coherent bunch center oscillation, multi-electron particles can be set in simulation. However, it is still the *Bassetti – Erskine* model applied to get the Coulomb force among ions and electrons. As pointed out, the ions distribution usually does not follow a Gaussian distribution. In the future, a Poisson solver based on the Particle-In-Cell methods can be added to this beam-ion module to handle the problem of self-consistence in the 'strong-strong' simulation.

4.6 Bunch-by-bunch feedback

The bunch-by-bunch feedback samples the beam transverse or longitudinal centroid information in the bunch-by-bunch sense [22, 23]. Passing these position signals through a FIR filter, the feedback creates bunch-by-bunch momentum kicks to the beam. A well-designed FIR filter in the bunch-by-bunch feedback has a zero amplitude response at the frequency nf_0 (DC rejection), so that the components caused by the closed orbit distortions, unequal bunch signal shapes from pickup electrodes, reflection at cable connections, *etc*, are filtered out. The information of the current turn is dropped off in general, indicating a one-turn delay $a_0 = 0$. The first derivatives of the phase response curves at the fraction of the target betatron tune νf_0 is usually designed to be zero to enlarge the phase error tolerance. The normalized amplitude response at the target tune fraction is a local minimum. The stable working region is limited by the filter phase response curve within $(-\pi, 0)$.

In Ref. [23], Nakamura shows that the time domain least square-fitting (TDLSF) method is a powerful tool to get the coefficients a_k for a FIR filter design. The oscillation of the beam at the k th turn is approximated by

$$\begin{aligned} x[k] &= \sum_{m=0}^M A^m \cos((1 + \Delta_k^m)\phi_k^m + \psi^m) \\ &\approx \sum_{m=0}^M (P_0^m \cos(\phi_k^m) + P_1^m \phi_k^m \sin(\phi_k^m) + Q_0^m \sin(\phi_k^m) + Q_1^m \phi_k^m \sin(\phi_k^m)) \end{aligned} \quad (40)$$

where M is the number of oscillation of the beam, A^m is the amplitude, ϕ_k^m and $(1 + \Delta^m)\phi_k^m$ are the assumed and actual phase advance at the k th turn, P and Q are undefined

parameters. In the same way, the output of the filter at current turn can be found

$$y[0] = \sum_{m=0}^M G^m (P_0^m \cos(\varphi^m + \zeta^m) + P_1^m \varphi^m \sin(\varphi^m + \zeta^m) + Q_0 \sin(\varphi^m + \zeta^m) + Q_1^m \varphi^m \cos(\varphi^m + \zeta^m)) \quad (41)$$

where G^m and ζ^m are the required gain and phase shift for the feedback, φ^m is the assumed phase advance from BPM to kicker. The FIR coefficients connects $x[k]$ to $y[0]$ with the required values of G^m , ζ^m , φ^m and ϕ_k^m . Applying the fitting function as $S = \sum_{k=0}^N (x[-k] - x_{-k})^2$, the least square fitting method would reduced to the condition

$$\frac{\partial S}{\partial P_i^m} = \frac{\partial S}{\partial Q_i^m} = 0, \quad (42)$$

by which the FIR coefficient a_k can be finally found.

Following this TDLSF method, a preliminary 10-tap FIR filter is designed, in the transverse directions for the PETRA-IV storage ring. Fig. 20 shows the filter coefficients, the phase and amplitude responses as functions of the tune fractions. In the simulation study, the pickup and kicker are located at the same place which means the phase responses of the filter at the target tunes have to be $-\pi/2$. If the maximum power P_{max} and the kicker impedance Z_{kicker} are specified in the input file, the kicker voltage will be limit to $\sqrt{P_{max} Z_{kick}}$.

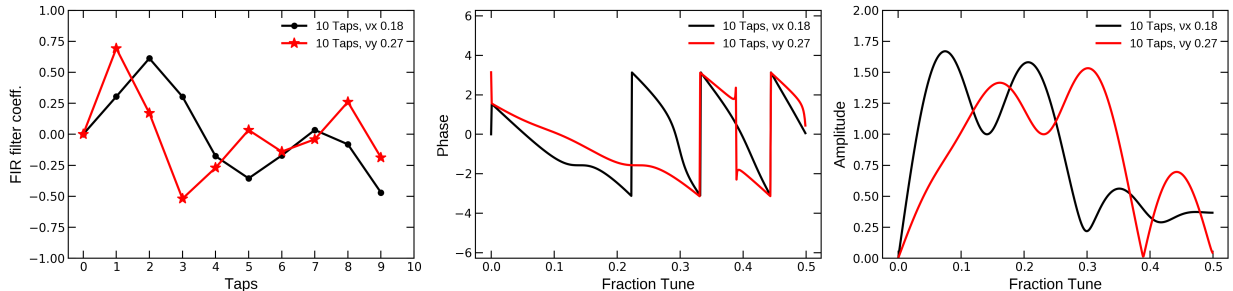


FIG. 20. The horizontal and vertical 10-tap FIR filter coefficients a_k (left), the frequency response of phase (middle) and amplitude (right). The horizontal and vertical target tune fractions are 0.18 and 0.27.

Figure 21 shows the comparison of the transverse coupled bunch mode growth rate due to the RW wakes with and without bunch-by-bunch feedback. The simulation conditions are the same as those applied in Fig. 9. The 10 taps FIR filter bunch-by-bunch feedback shown

in Fig. 20 is also applied in tracking. All modes are suppressed as expected. With the same beam condition, we also give the motions of the 80 bunch centroids in the "grow-damped" simulation in Fig. 22. During the tracking, the bunch-by-bunch feedback is turned on from 1000 to 1300 turns and from 1600 to 3000 turns. Clearly, without the feedback, the bunches are unstable due to the transverse long-range RW wakes. When the bunch-by-bunch feedback is turned on, oscillations of all of the bunches can be stabilized to zero.

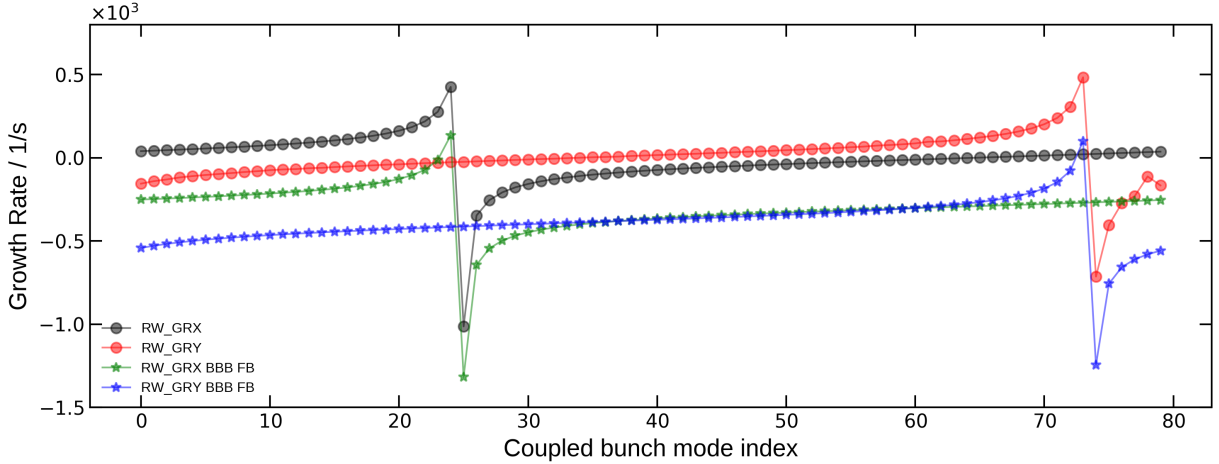


FIG. 21. Comparison of the transverse coupled bunch growth rate due to the RW with and without bunch-by-bunch feedback. The simulation condition is the same as those applied in Fig. 9. The 10 taps bunch-by-bunch feedback shown in Fig. 20 is applied in tracking.

4.7 Emittance exchange and linear coupling

Skew quadrupole lead to a coupling effect between the horizontal and vertical planes, which re-distributes the equilibrium emittances together with the synchrotron radiation damping and quantum-excitation effects. Here, we note K as the skew quadrupole strength with dimension $1/m$. In Ref. [24], Lindberg shows a model to predict the equilibrium emittance as function of the difference of fraction tune Δ_r ,

$$\epsilon_x = \epsilon_0 \frac{1 + \frac{1}{4\tau_x}(\tau_y - 3\tau_x) \sin^2 \theta}{1 + \frac{1}{4\tau_x \tau_y}(\tau_x - \tau_y)^2 \sin^2 \theta} \quad \epsilon_y = \epsilon_0 \frac{\frac{1}{4\tau_x}(\tau_y + \tau_x) \sin^2 \theta}{1 + \frac{1}{4\tau_x \tau_y}(\tau_x - \tau_y)^2 \sin^2 \theta} \quad (43)$$

where, $\sin^2 \theta = \frac{\kappa^2}{\kappa^2 + \Delta_r^2}$ and $\kappa = \sqrt{\frac{\beta_x \beta_y}{4\pi^2} K^2}$ is the linear coupling coefficient. If the working tune smoothly crosses the difference resonance, the emittance would exchange between the

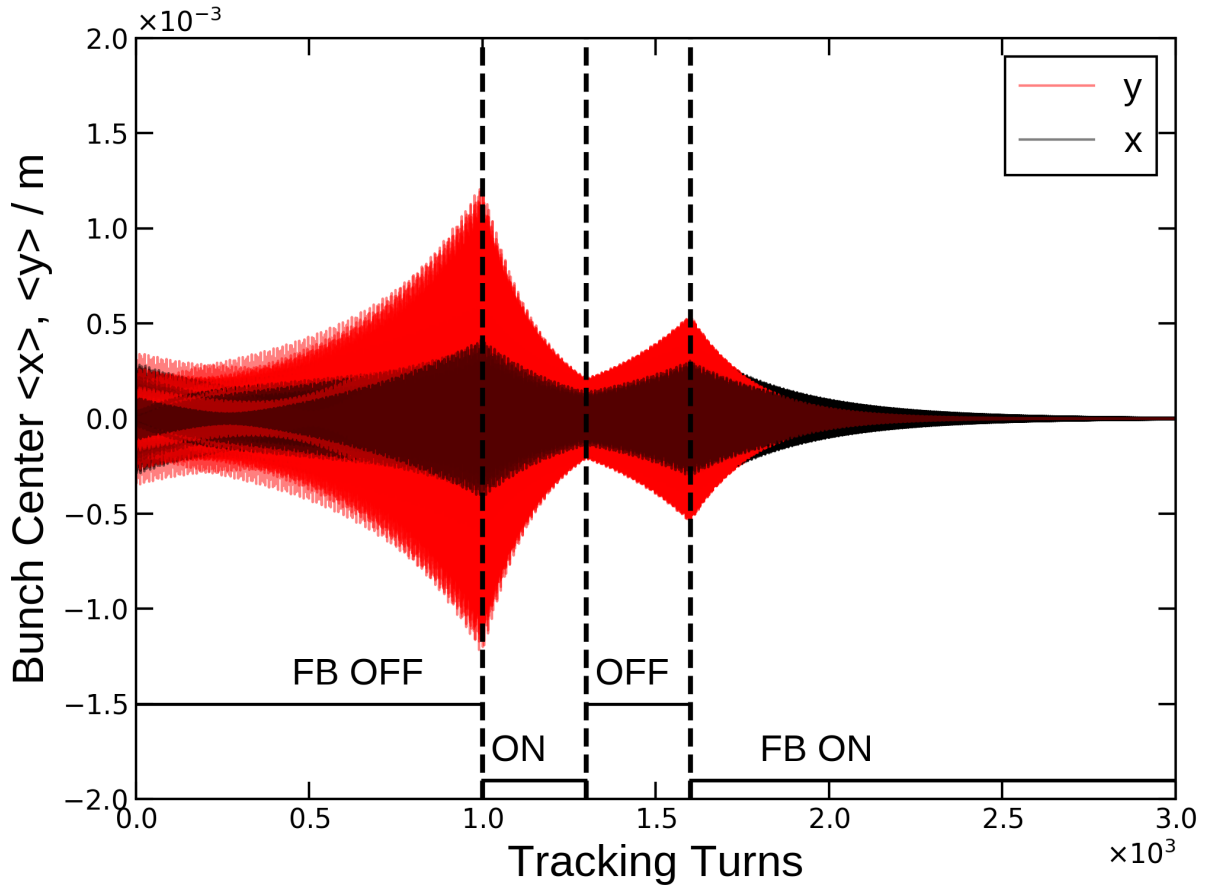


FIG. 22. Trajectories of the 80 bunches centroids. The bunch-by-bunch feedback is turned on from 1000 to 1300 turns and from 1600 to 3000 turns during tracking. The long-range RW wakes are turned on during the whole simulation.

horizontal and vertical planes due to this linear coupling.

To study the effect, an extra skew quadrupole can be set beside the one-turn transfer map Eq. 2 in CETASim. Both the strength of the skew quadrupole and the working tunes can be set as ramping variables as a function of the tracking turns. We give two cases for linear coupling studies. The first one is the static case in which all the lattice parameters are fixed during tracking. The second one is the dynamical cases, during which the difference resonance is crossed by ramping the working tune. Still, the nominal settings of the PETRA-IV lattice and beam condition are applied as the initial conditions. Fig. 23 shows the simulation results from CETASim. The left sub-figure shows the final equilibrium emittance as a function of tune difference in the static simulation. The skew quadrupole

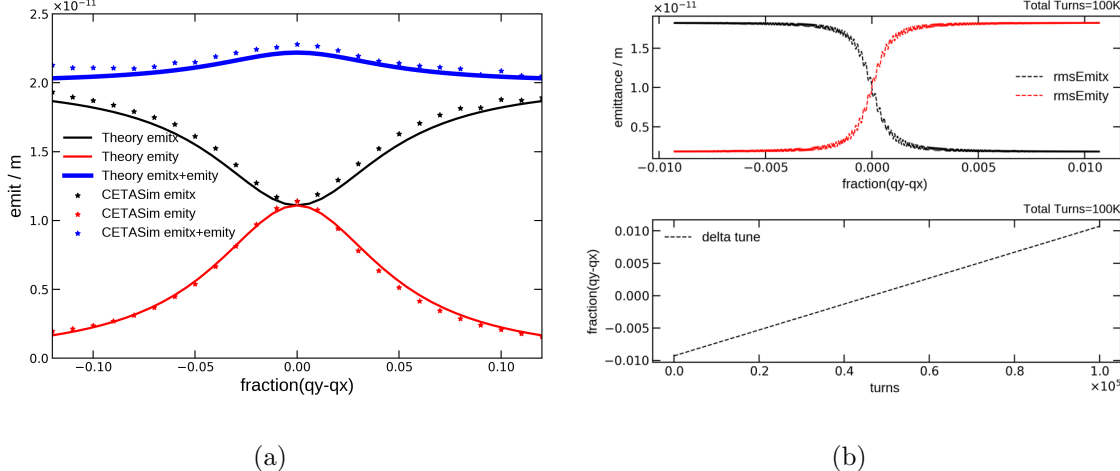


FIG. 23. Left: equilibrium emittance as function of distance to difference resonance. Right: how the horizontal and vertical emittance are exchanged when the difference resonance is smoothly crossed in $1.E+5$ turns.

strength is set as $0.05 \text{ } 1/m$. Compared to the predictions from Eq. 43, tracking results show a very good agreement. The sub-figure on the right shows how the horizontal and vertical emittance are exchanged when the difference resonance is smoothly crossed. The skew quadrupole strength is set to $5 \times 10^{-4} \text{ } 1/m$, and the vertical tune ramps from 0.17 to 0.19 within 10^5 turns.

5 SUMMARY AND OUTLOOK

In the paper, the code CETASim, developed recently, is introduced in detail. The motivation of CETASim development is to have a simulation tool that covers the collective effects in electron storage rings, especially when different filling pattern schemes are of great concern. The charge of the bunches can be set differently to study the effects from “guard bunches” which normally used for transient beam loading compensation and ions cleaning. The architecture of the code is carefully designed so that one can easily expand it if other beam dynamics have to be taken into account. Instead of the element-by-element tracking method, CETASim takes the one-turn transfer map for simplicity, where the amplitude-dependent tune shift and the momentum compaction factor can be taken into account up to the second order. Currently, CETASim includes modules to study the single bunch effects, coupled-bunch effects, transient beam loading, beam-ion effects and

bunch-by-bunch feedback. These modules are well benchmarked with results from the theoretical predictions and tracking in Elegant. For the study of the transient beam loading, the coupled generator dynamics and beam dynamics are treated self-consistently. The coupled-bunch instability can be subtly turned off in tracking, which is not physical, however, it can help the user to get the first idea about how different bunches are lengthened due to different filling patterns.

Still, there are several things to be upgraded in the future. The first one is to have a subroutine that can import the external short-range and long-range wakes in general for the beam dynamics simulation. As we mentioned in the manuscript, for the single bunch effect, CETASim takes the impedance as the green function; and for the coupled bunch effect, the long-range wakes are limited to the analytical RW and RCL models. The second one is to have a module to simulate the cavity feedback self-consistently. At this moment, a very simple ideal cavity feedback is available. In the future, we will update the cavity feedback module to cover the real experiment setups with the help of the low-level RF group. The third one is the Coulomb interaction between electrons and ions. The *Bassetti – Erskine* formula based on the 2D Gaussian distribution function is not an accurate approach to get the Coulomb force among the ions and electrons. A self-consistent PIC subroutine will be developed to handle this problem. Finally, we plan to improve the performance of CETASim including algorithm optimization and parallelization in the future.

6. ACKNOWLEDGEMENTS

The authors would like to thank Dr. Mikhail Zobov from INFN in Frascati for helpful discussions. We would like to thank Dr. Sergey Antipov as well for proofreading the manuscript and providing numerous helpful comments and suggestions. This work is supported by the European Union’s Horizon 2020 research and innovation program under grant agreement No. 871072.

* chao.li@desy.de

† yong-chul.chae@desy.de

[1] https://ops.aps.anl.gov/manuals/elegant_latest/elegant.html.

- [2] G. Skripka, R. Nagaoka, M. Klein, F. Cullinan, and P. F. Tavares, “Simultaneous computation of intrabunch and interbunch collective beam motions in storage rings,” *Nuclear Instruments and Methods in Physics Research Section A: Accelerators, Spectrometers, Detectors and Associated Equipment*, vol. 806, pp. 221–230, 2016.
- [3] <https://github.com/PyCOMPLETE/PyHEADTAIL>.
- [4] <https://ops.aps.anl.gov/manuals/SDDStoolkit/SDDStoolkit.html>.
- [5] K. Hirata, “BBC User’s Guide: A Computer Code for Beam-Beam Interactions with a Crossing Angle, Version 3.4,” *CERN SL-Note-97-57-AP*, 1997.
- [6] A. W. Chao, “Physics of collective beam instabilities in high energy accelerators,” *Wiley*, 1993.
- [7] K. Yokoya, “Resistive wall impedance of beam pipes of general cross section,” *Part. Accel.*, vol. 41, no. KEK-Preprint-92-196, pp. 221–248, 1993.
- [8] M. Bassetti and G. A. Erskine, “Closed expression for the electrical field of a two-dimensional Gaussian charge,” *CERN Report*, 1980.
- [9] To avoid the numerical divergence, in CETASim, Eq. 22 is de-generates to the 1D Gaussian model when $\text{abs}((\sigma_x - \sigma_y)/\sigma_y) < 10^{-4}$.
- [10] P. Wilson, “Fundamental-mode rf design in e+ e- storage ring factories,” *Springer*, pp. 293–311, 1994.
- [11] T. Schilcher, “Vector sum control of pulsed accelerating fields in Lorentz force detuned superconducting cavities.,” *Ph. D. Thesis, Hamburg University*, 1998.
- [12] Smooth approximation or slow variation approximation.
- [13] T. Berenc, M. Borland, and R. Lindberg, “Modeling rf feedback in elegant for bunch-lengthening studies for the advanced photon source upgrade,” *Proc. of IPAC15, MOPMA006*, 2015.
- [14] In the study of transient beam loading effect, the cos convention is adopted, whereas in Eq. 1, it is sin convention.
- [15] <https://bib-pubdb1.desy.de/record/426140/files/DESY-PETRAIV-Conceptual-Design-Report.pdf>.
- [16] https://gitlab.com/IRIS_mirror/IW2D_mirror.
- [17] W. Bruns, “Gdfidl on massive parallel systems,” *Proc. of Linac*, pp. 416–418, 2002.

- [18] G. Rehm, M. Abbott, and A. Morgan, “New features and measurements using the upgraded transverse multibunch feedback at diamond,” *Proc. IBIC’14*, pp. 696–699, 2014.
- [19] D. Boussard, “Beam loading (particle accelerators),” 1995.
- [20] C. Li, S. Tian, N. Wang, and H. Xu, “Beam-ion instability and its mitigation with feedback system,” *PRApB*, vol. 23, no. 7, p. 074401, 2020.
- [21] L. Wang, Y. Cai, T. O. Raubenheimer, and H. Fukuma, “Suppression of beam-ion instability in electron rings with multibunch train beam fillings,” *Phys. Rev. ST Accel. Beams*, vol. 14, p. 084401, Aug 2011.
- [22] M. Lonza, “Multi-bunch feedback systems,” *Cern Accelerator School 2013*, 2008.
- [23] T. Nakamura, “Single-loop Multi-Dimensional Digital Feedback by FIR Filters,” *Spring-8, Japan*, 2009.
- [24] R. Lindberg, “Equilibrium emittances of coupled lattices including intrabeam scattering,” *AOP-TN-2014-020*, 2014.